HHS Public Access

Author manuscript

Immunity. Author manuscript; available in PMC 2024 December 12.

Published in final edited form as:

Immunity. 2023 December 12; 56(12): 2736–2754.e8. doi:10.1016/j.immuni.2023.11.001.

Nuclear localization of STING1 competes with canonical signaling to activate AHR for commensal and intestinal homeostasis

Ruoxi Zhang[1], **Chunhua Yu**[1], **Herbert J Zeh**[1], **Haichao Wang**[2], **Guido Kroemer**[3,4,5], **Daniel J. Klionsky**[6], **Timothy R Billiar**[7], **Rui Kang**[1,*], **Daolin Tang**[1,8,*]

[1]Department of Surgery, UT Southwestern Medical Center, Dallas, Texas 75390, USA

[2]Laboratory of Emergency Medicine, North Shore University Hospital and the Feinsteins Institute for Medical Research, Manhasset, NY 11030, USA

[3]Centre de Recherche des Cordeliers, Equipe labellisée par la Ligue contre le cancer, Université de Paris, Sorbonne Université, INSERM U1138, Institut Universitaire de France, Paris, France

[4]Metabolomics and Cell Biology Platforms, Gustave Roussy Cancer Campus; 94800 Villejuif, France

[5]Pôle de Biologie, Hôpital Européen Georges Pompidou, AP-HP; 75015 Paris, France

[6]Life Sciences Institute and Department of Molecular, Cellular and Developmental Biology, University of Michigan, Ann Arbor, MI 48109, USA

[7]Department of Surgery, University of Pittsburgh, Pittsburgh, PA 15219, USA

[8]Lead contact

SUMMARY

Extensive studies demonstrate the importance of the STING1 protein as a signaling hub that coordinates immune and autophagic responses to ectopic DNA in the cytoplasm. Here, we report a nuclear function of STING1 in driving the activation of the transcription factor AHR to control gut microbiota composition and homeostasis. This function was independent of DNA sensing and autophagy and showed competitive inhibition with cytoplasmic cGAS-STING1 signaling. Structurally, the cyclic dinucleotide binding domain of STING1 interacted with the AHR N-terminal domain. Proteomic analyses revealed that STING1-mediated transcriptional activation of AHR required additional nuclear partners, including positive and negative regulatory proteins.

*Correspondence: daolin.tang@utsouthwestern.edu (D.T.) and rui.kang@utsouthwestern.edu (R.K.).

AUTHOR CONTRIBUTIONS

R.Z., D.T., and R.K. conceived and planned the experiments. R.Z., C.Y., D.T., and R.K. carried out the simulations and sample preparation and analyzed the data. R.Z. and D.T. wrote the paper. D.T., and R.K. provided research fundings. H.J.Z. and T.R.B provided experimental reagents. H.J.Z., H.W., G.K., D.J.K., and T.R.B assisted in data interpretation and edited the manuscript.

DECLARATION OF INTERESTS

The authors have no competing interests to declare.

Although AHR ligands could rescue colitis pathology and dysbiosis in wild type mice, this protection was abrogated by mutational inactivation of STING1. These findings establish a key framework for understanding the nuclear molecular crosstalk between the microbiota and the immune system.

eTOC Blurb

The impotance of STING1 in innate interferon responses to intracellular nucleotids is well known. Here, Zhang et al. show that, in contract to its cytoplasmic functions, STING1 can localize to the nucleus to drive activation of the transcription factor, AHR. Nuclear STING-AHR interactions protect mice against intestinal pathology and dysbiosis.

Graphical Abstract

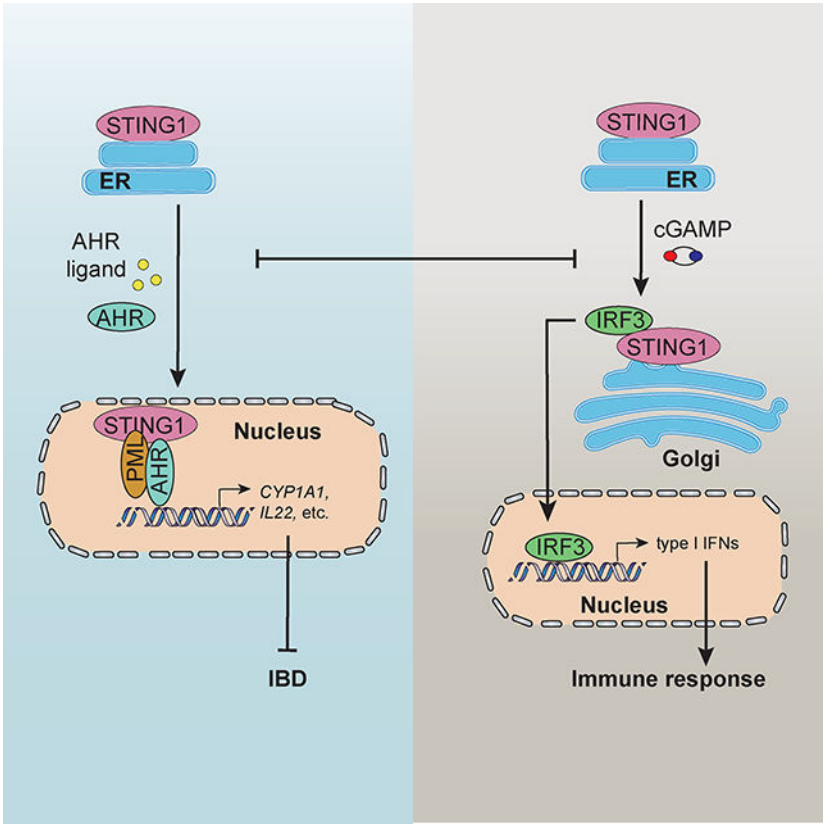

INTRODUCTION

STING1 (stimulator of interferon response cGAMP interactor, also known as STING or TMEM173) is an evolutionarily conserved transmembrane protein expressed in immune and non-immune cells. STING1 is as an endoplasmic reticulum (ER)-associated protein that mediates immune defense against infection by pathogens that contain DNA or produce DNA during their life cycle[1–4]. CGAS (cyclic GMP-AMP synthase) acts as a cytosolic DNA sensor that produces the second messenger cyclic guanosine monophosphate-adenosine monophosphate (cGAMP)[5–7], which together with bacterial cyclic dinucleotides (CDNs),

activate STING1, resulting in STING1 oligomerization and translocation to the Golgi apparatus via the ER-Golgi intermediate compartment (ERGIC)[8–11]. At the Golgi, STING1 recruits TBK1 (TANK binding kinase 1) that activates IRF3 (interferon regulatory factor 3)-mediated transactivation of type I IFNs (interferons) and also stimulates the NFKB (NF-κB nuclear factor kappa B)-driven production of inflammatory cytokines (e.g., TNF [tumor necrosis factor] and IL6 [interleukin 6])[12–16]. Accumulating evidence reveals other IFN-independent functions of STING1 in regulating autophagy and cell death at different cellular organelles[17–19]. An improved understanding of the subcellular localization and function of STING1 may be important for developing effective immunotherapeutic strategies.

AHR (aryl hydrocarbon receptor) is a ligand-activated transcription factor that senses dietary, microbial, and metabolic signals [20]. In the intestine, AHR is expressed by immune, epithelial, and endothelial cells, ensuring homeostasis between the host and gut microbiota[21,22]. Under normal conditions, AHR is located in the cytoplasm in a complex with molecular chaperones, such as heat shock protein 90 (HSP90). Upon ligand binding, the AHR-chaperone complex undergoes conformational changes and consequently translocates into the nucleus, resulting in the release of AHR from HSP90. Nuclear AHR then heterodimerizes with ARNT/HIF-1β (aryl hydrocarbon receptor nuclear transporter) protein to initiate transcription of AHR target genes, especially *CYP1A1* (cytochrome P450 family 1 subfamily A member 1). Impaired AHR signaling has detrimental effects on the survival and function of intestinal immune cells and predisposes to inflammatory diseases, including inflammatory bowel disease (IBD) [23].

Here, we conducted a transcriptome analysis comparing wild-type (WT) and *Sting1*$^{Gt/Gt}$ mice (which lack expression of functional STING1[24–26]) and identified STING1 as a regulator of AHR activation independent of its classical functions in mediating type I IFN production and autophagy induction. STING1 directly controled transcriptional activity of AHR in the nucleus, rather than affecting AHR activation in the cytoplasm. Subsequent mutagenesis and molecular studies unraveled the structural basis of these interactions, as well as cofactors that regulate gene transcription by the STING1-AHR protein complex. In mouse models of IBD, the loss of *Sting1* attenuated AHR ligand-mediated protection of the gut microbiota and innate immunity. Thus, nuclear STING1 possesses widespread IFN-independent activities that are important for controlling intestinal immunity and microbial homeostasis.

RESULTS

STING1 mediates AHR activation

STING1 deficiency leads to impaired mucin secretion and disruption of intestinal homeostasis[27]. To explore these effects at the mechanistic level, we compared colon tissues from WT mice and *Sting1*$^{Gt/Gt}$ mice by whole-transcriptome RNA sequencing (Fig. 1A). Gene ontology (GO) analysis of differentially expressed genes showed that pathways related to lipid metabolism or CYP (cytochrome P450 family)-related metabolism were reduced in *Sting1*$^{Gt/Gt}$ mice (Fig. 1B, S1A, and S1B). As an internal control, inactivation of STING1 compromised the calcium signaling pathway consistent with its important role in the regulation of calcium homeostasis[28,29].

AHR is a transcription factor and xenobiotic receptor regulating lipid metabolism and xenobiotic metabolism[30,31]. To determine whether STING1 promotes CYP-related xenobiotic metabolism in an AHR-dependent fashion, we assessed the induction of the representative AHR-target genes *CYP1A1* and *IL22* (*interleukin 22*) in response to classical tryptophan-derived AHR ligands (e.g., 6-formylindolol[3,2-b]carbazole [FICZ], 2-[1'H-indole-3'-carbonyl]-thiazole-4-carboxylic acid methyl ester [ITE], and β-anthraniloyl-L-alanine [L-KYN]) in WT and STING1-deficient cells, including THP1 (human monocytic cell line), HT-29 (human colorectal adenocarcinoma cell line), mouse embryonic fibroblasts (MEFs), mouse primary peritoneal macrophages, and mouse T helper 17 (Th17) cells differentiation from naïve CD4 T lymphocytes. The deficiency of *STING1* blocked the AHR ligand-induced *CYP1A1* and *IL22* (Fig. 1C, 1D, S1C–S1H, and Table S1). The re-expression of STING1 restored *CYP1A1* and *IL22* induction in STING1-deficient cells following the treatment with AHR ligands (Fig. 1E, 1F, S1J, and S1K). In contrast, AHR ligands did not induce *STING1* mRNA expression (Fig. S1I). These findings suggest that STING1 acts as a positive regulator of ligand-dependent AHR activation.

We next determined whether STING1-mediated AHR activation requires the canonical functions of STING1 linked to type I IFN production or autophagy induction. Unlike the depletion of *STING1*, the deletion of *CGAS* or *IRF3* and the overexpression of IFN-independent STING1 mutants (S366A and L374A) did not impact *CYP1A1* induction by AHR ligands in THP1 cells[32] (Fig. 1G and S1L). Moreover, the AHR ligand-induced *CYP1A1* expression was unaffected by the deletion of the essential autophagy gene *Atg5* (*autophagy related 5*) in MEFs (Fig. 1H and 1I). As a positive control, the generation of MAP1LC3A/B (microtubule-associated protein 1 light chain 3 alpha/beta)-II, a marker of autophagosomes, was inhibited in *Sting1*$^{-/-}$ and *Atg5*$^{-/-}$ MEFs (Fig. 1H and 1I). Consistent with previous studies[33,34], high doses of AHR ligands reduced cell viability, and this lethal process was enhanced by the depletion of *STING1* in THP1 cells and MEFs (Fig. 1J). These findings suggest that STING1 promotes AHR activation independent of its known canonical functions in mediating CGAS responses or stimulating autophagy.

Nuclear STING1 promotes AHR activation

Next, we assessed the mechanisms by which STING1 regulates AHR activation by examining the effect of STING1 on two critical steps of AHR-mediated gene transcription, namely (i) the nuclear translocation of AHR and (ii) the release of AHR from the AHR-HSP90 complex[20] (Fig. 2A). Cellular fractionation analysis combined with immunofluorescence analysis revealed that ITE-induced AHR accumulation in the nucleus peaked at 1 h in THP1 and MEF cells; however, STING1 deficiency did not affect ITE-induced nuclear translocation of AHR (Fig. 2B, 2C, and S2A–S2B). Immunoprecipitation experiments showed that *STING1* depletion did not affect the ITE- or L-KYN-induced dissociation of the AHR-HSP90 complex (Fig. 2D and S2C). These data exclude the possibility that STING1 is required for the nuclear translocation of AHR and its release from molecular chaperones.

STING1 is mainly expressed in the ER, with a small amount of basal expression in other subcellular organelles [35]. We found that nuclear STING1 expression increased after

AHR ligand exposure (Fig. 2B and S3B). Cellular fractionation experiments confirmed that AHR ligands (ITE and L-KYN) induced the accumulation of STING1 and AHR proteins in the nucleus and simultaneously reduced their abundance in the cytoplasm compared to vehicle DMSO control (Fig. 2E). The canonical STING1 ligand 2'3'-cGAMP, which induces type I IFN production, failed to induce nuclear STING1 accumulation (Fig. 2E). Immunofluorescence analysis confirmed that ITE and L-KYN increased the nuclear accumulation of STING1 and colocalization of STING1 with nuclear envelope marker LMNA (lamin A/C) (Fig. 2F and S2D). As a positive control, 2'3'-cGAMP triggered the colocalization of STING1 and the ERGIC marker LMAN1/ERGIC53 (lectin, mannose binding 1) in the cytosol without any nuclear translocation of STING1 (Fig. 2F and S2D).

To examine whether nuclear STING1 is required for AHR activation, we characterized cells expressing mutated STING1 and used pharmacological inhibitors to alter the subcellular localization of STING1. Two STING1 mutations (V155M and N154S) cause constitutive STING1 expression in the ERGIC and subsequent TBK1 and IRF3 activation[28,36]. Brefeldin A inhibits STING1 accumulation in ERGICs[11], whereas H-151 limits the palmitoylation of STING1 to prevent the localization of STING1 at the Golgi apparatus[37] (Fig. 2G). The AHR ligand ITE induced less *CYP1A1* mRNA in THP1 cells expressing V155M- and N154S-mutated STING1; however, such cells produced more type I IFN than their WT counterparts (Fig. 2H and S2E). Furthermore, brefeldin A (but not H-151) improved *CYP1A1* production in ITE-stimulated WT cells, as well as in V155M and N154S mutant cells (Fig. 2I). These findings indicate that the exit of STING1 from the ER may impair STING1-mediated AHR activation.

To further test our hypothesis that ER-to-ERGIC translocation of STING1 impairs AHR activation, we analyzed the effect of the N154S mutation on the nuclear translocation of STING1 in response to AHR ligands. Mutant STING1^{N154S} remained in the cytoplasm upon AHR ligation, contrasting with WT STING1 that translocated to the nucleus (Fig. S2G). In contrast, the nuclear accumulation of AHR occurred in cells expressing ERGIC-located (V155M and N154S) and WT STING1 to the same degree (Fig. 2J). Altogether, STING1 regulates AHR activation through its nuclear localization.

Competitive inhibition between canonical and non-canonical pathways of STING1

Based on the aforementioned results (Fig. 2), we hypothesized that the canonical cGAMP-elicited STING1 pathway (initiated in the ER and ERGIC) is incompatible with the AHR-relevant non-canonical pathway (requiring nuclear translocation of STING1), resulting in a "competition" for STING1 action. To test this possibility, THP1 cells were stimulated with ITE and/or 2'3'-cGAMP for the indicated times (Fig. 3A), and their effects on *CYP1A1* expression and type I IFN induction were examined. By itself, ITE induced CYP1A1 expression without activating the type I IFN pathway; however, simultaneous treatment with ITE and 2'3'-cGAMP inhibited *CYP1A1* induction (Fig. 3B and 3C). Conversely, 2'3'-cGAMP alone induced the phosphorylation of STING1 and IRF3 as well as the production of *IFNB1* (interferon beta 1) and this effect was inhibited by co-treatment with ITE (Fig. 3B and 3C). Similarly, 2'3'-cGAMP and ITE co-treatment inhibited ITE-induced *Cyp1a1* expression and 2'3'-cGAMP-induced *Ifnb1* expression in primary peritoneal macrophages

(Fig. S3A and S3B). These findings support a competitive relationship between the STING1-AHR pathway and the CGAS-STING1-IRF3 pathway.

Considering our observation that the constitutive ERGIC accumulation of STING1 impairs STING1 nuclear localization and subsequent AHR activation (Fig. 2), we investigated whether AHR activation conversely suppresses the CGAS-STING1 pathway activation by altering STING1 location. Non-reducing and native PAGE analysis demonstrated that ITE inhibited 2'3'-cGAMP-induced phosphorylation of STING1 and TBK1, which occurs at the Golgi; however, ITE failed to affect STING1 polymerization, which occurs at a prior step between ligand-binding and ERGIC-translocation of STING1[8] (Fig. 3D). ITE disrupted the 2'3'-cGAMP-induced cytoplasmic accumulation of STING1 and instead promoted its accumulation in the nucleus (Fig. 3E). Mutations (e.g., R281Q) that induce STING1 polymerization can constitutively activate STING1 and trigger the production of downstream type I IFNs[8,38,39]. We found that the R281Q mutation inhibited ITE-induced *CYP1A1* production and STING1 nuclear translocation (Fig. S3D and S3E), whereas promoted STING1 polymerization and TBK1 phosphorylation for the activation of the CGAS-STING1 pathway (Fig. S3C). These findings support our hypothesis that nuclear translocation of STING1 limits the activation of the CGAS-STING1-IRF3 pathway by sequestering STING1 away from the ERGIC, while ER-exit of STING1 restricts the AHR-STING1 pathway activation by preventing nuclear accumulation of STING1.

We further investigated STING1 as a "switch" between the AHR and type I IFN pathways using a strategy of ligand-occupancy stimulation. Pulse treatment with ITE for 1 h inhibited the 2'3'-cGAMP-induced phosphorylation of STING1 and phosphorylation of IRF3 (Fig. S3F), as well as *IFNB1* production (Fig. 3F and 3G). In contrast, pulse treatment with 2'3'-cGAMP for 1 h before ITE treatment reduced ITE-induced *CYP1A1* expression (Fig. 3H and 3I). Thus, the pool of ER-located STING1 protein may be alternatively mobilized to contribute to the AHR and type I IFN pathways, depending on its subsequent translocation to other cellular compartments. Besides, pulse treatment of cGAMP with addition of ITE induced partial phosphorylation of STING1, phosphorylation of IRF3, and production of *IFNB1*, whereas pulse treatment of ITE with addition of cGAMP only induce slight *CYP1A1* expression (Fig. S3G–S3I). Furthermore, the protein-drug docking analysis showed that AHR ligands could bind to transmembrane (TM) domain of STING1, in contrast to 2'3'-cGAMP, which binds to the CDN binding domain (CBD) (Fig. S3J). The analysis of protein-drug binding using cellular thermal shift assay (CETSA) [40], demonstrated that 2'3'-cGAMP was more effective at stabilizing STING1 compared to the AHR ligand (Fig. S3K), indicating a higher affinity of 2'3'-cGAMP for STING1. However, AHR deficiency did not significantly reduce the nuclear translocation of STING1 induced by AHR ligands in THP1 cells (Fig. S3L). Altogether, these findings suggest that STING1 preferentially functions in the CGAS-STING1 pathway, rather than in the AHR pathway, consistent with the amount of STING1 remaining cytoplasmic upon AHR activation (Fig. 2E, 2F, and 3E).

Structural basis of STING1-AHR complex formation

Considering that STING1 and AHR colocalized in the nucleus upon activation, we examined whether STING1 physically interacts with AHR in this compartment. In untreated THP1 cells, AHR coimmunoprecipitated with STING1 (Fig. 4A). This association was increased by prior culture in the presence of AHR ligands and decreased upon exposure to 2'3'-cGAMP. To further support the physical interaction between STING1 and AHR, hemagglutinin (HA)-tagged AHR was co-immunoprecipitated with FLAG-tagged STING1 in human embryonic kidney (HEK293T) cells (Fig. 4B).

STING1 protein contains an N-terminal transmembrane (TM) domain that spans the ER membrane four times, a dimerization domain (DD) that mediates the formation of the STING1 dimer, a cytosolic CDN binding domain (CBD) that binds to ligands, an unfolded protein response (UPR) domain that regulates ER stress and autophagy, and a C-terminal tail (CTT) that interacts with, and activates, TBK1 and IRF3 (Fig. 4C)[13,17,28,41,42]. To determine which domain of STING1 is responsible for AHR interaction, we performed coimmunoprecipitation assays using lysates of HEK293T cells overexpressing full-length STING1 or alternatively truncated mutants (Fig. 4D). STING1 mutants that retained the CBD (AA 180–321) interacted with AHR, whereas mutants lacking the CBD completely lost this interaction. In addition, compared to full-length STING1, the mutant truncated at the N-terminal TM domain (AA 140–379) exhibited an enhanced interaction with AHR (Fig. 4D).

AHR is composed of an N-terminal basic helix-loop-helix (bHLH) domain required for DNA binding, followed by two Per-ARNT-Sim (PAS) domains (A and B) required for ligand binding and protein interaction and a C-terminal transactivation domain (TAD) that activates or blocks transcription of target genes (Fig. 4E)[43,44]. To determine which domain of AHR interacts with STING1, we again performed coimmunoprecipitation using lysates of HEK293T cells overexpressing full-length AHR or truncated mutants. We found that the N terminus of AHR containing the bHLH and PAS domains was required for interaction with STING1 and AHR transcriptional activity, whereas the AHR mutant lacking the transactivation domain exhibited enhanced interaction with STING1 (Fig. 4F and S5D). Protein-protein docking analysis revealed that AHR Arg94 (R94) is a critical binding site that interacts with STING1 Gln266 (Q266) and Pro209 (P209), while STING1 R220 and R253 can form a 3D-cluster and interact with AHR Gln249 (Q249) and ILE258 (I258) (Fig. S4A). Immunoprecipitation assays further confirmed that mutations in AHR at R94, as well as in STING1 at R220 and R253, resulted in abnormal protein interaction between STING1 and AHR (Fig. S4B and S4C). These data suggest that the CBD of STING1 interacts with the N-terminal domains of AHR.

After translocation into the nucleus, AHR dimerizes with ARNT, an obligatory partner for its DNA-binding and functional activity. The AHR-ARNT dimer then binds to the promoters of AHR target genes and initiates gene transcription (Fig. 4G)[45–47]. We took advantage of HT-29 cells expressing a secreted luciferase reporter gene under the *CYP1A1* gene promoter (HT-29 lucia cells) to monitor the transcriptional activity of AHR and found that *STING1* deficiency blocked AHR-dependent gene transcription (Fig. 4H). The overexpression of full-length or mutant *STING1* containing the CBD similarly promoted AHR-mediated

transactivation of *CYP1A1*, whereas mutants lacking the CBD failed to do so (Fig. 4I, S4E, and S4F). These data suggest that AHR regulation of transcription requires the interaction of STING1 with AHR.

Given that the PAS domain mediates the dimerization of AHR with ARNT[48,49] and that STING1 binds to AHR mutants containing this domain, we speculated that STING1 might favor the generation of an active AHR-ARNT complex. However, immunoprecipitation revealed that the AHR ligands ITE and L-KYN induced the binding of endogenous AHR to ARNT and that this outcome was not affected by the depletion of *STING1* in THP1 cells (Fig. 4J).

Altogether, our findings suggest that STING1 interacts with AHR through its CBD and regulates AHR transcriptional activity without affecting its interaction with ARNT.

STING1 nuclear partners regulate AHR activation

The known binding partners of STING1 in the nucleus include transcriptional activators and co-activators[35,50]. The AHR PAS domain, which interacts with STING, is not only involved in dimerization with ARNT, but also contributes to the activity of AHR as a transcription factor[48,51,52]. Based on the finding that STING1 does not affect the AHR-ARNT interaction, we were intrigued by the possibility that STING1 might stimulate AHR function via other transcriptional activators.

Using nuclear IP combined with quantitative mass spectrometry, we identified the interactome of nuclear STING1 in THP1 cells cultured in the absence or presence of AHR ligands. A total of 365 candidate proteins were identified to interact with STING1 after treatment with ITE and L-KYN (Table S4). GO analysis of these candidate proteins revealed a series of transcription-related pathways affected by STING1 (Fig. 5A). Among the binding proteins related to the regulation of gene transcription, we focused on three potential transcriptional coactivators (DHX9 [DExH-box helicase 9], RNF20 [ring finger protein 20], and PML [PML nuclear body scaffold]) as well as DNA-binding protein XRCC6 (X-ray repair cross complementing 6) (Fig. 5B). DHX9 and XRCC6 were identified as binding partners of STING1 in previous reports[35,50]. Nuclear IP experiments confirmed that the interaction of these four candidates (DHX9, RNF20, PML, and XRCC6) with STING1 was increased during AHR activation (Fig. S5A). Only the *PML* deficiency impaired ITE-induced CYP1A1 expression, while the loss of *DHX9* or *XRCC6* inversely promoted ITE-induced CYP1A1 in THP1 (Fig. 5C) and HT-29 (Fig. S5B) cells. PML deficiency also inhibited L-KYN-induced CYP1A1 expression (Fig. S5C). Consistently, the transcriptional activity elicited by AHR ligands was reduced in PML-deficient HT-29 lucia cells (Fig. 5D). These data confirm that PML promotes AHR activation, contrasting with DHX9 or XRCC6 that inhibit AHR activation.

We then analyzed protein-protein interactions among STING1, PML, and AHR. The association of PML with AHR was increased in THP1 and HT-29 cells after ITE or L-KYN stimulation, and STING1 deficiency led to decreased PML-AHR interaction, rather than affecting PML protein expression (Fig. 5E, S5D, and S5E). Conversely, the overexpression of STING1 increased the binding of PML and AHR (Fig. 5F), indicating that STING1 may

act as a scaffolding protein to favor the formation of the AHR-PML transcriptional complex (Fig. 5G).

We also investigated whether DHX9 or XRCC6 inhibited AHR activation in a STING1-dependent manner. Indeed, the loss of *DHX9* or *XRCC6* did not restore ITE-induced *CYP1A1* expression in *STING1* KO THP1 cells (Fig. S5F). However, the loss of *DHX9* or *XRCC6* enhanced the abundance of AHR and STING1 proteins with or without ITE treatment (Fig. S5G), suggesting that DHX9 and XRCC6 may regulate the protein stability of AHR and STING1 independently of stimulation by AHR ligands. To address this hypothesis, a cycloheximide chase analysis of protein half-life was performed. AHR expression rapidly decreased after the inhibition of protein synthesis, and this process was delayed by the silence of *DHX9* or *XRCC6* (Fig. S5H).

Collectively, we demonstrated that nuclear STING1 not only recruits the transcriptional activator PML to enhance AHR transcriptional function, but also binds to DHX9 and XRCC6, thus preventing the activation of AHR.

STING1 is required for AHR-mediated IBD protection in mice

AHR can be activated by short-chain fatty acids or dietary and microbial tryptophan metabolites to induce the production of anti-inflammatory cytokines, promote barrier tissue restoration, and maintain microbial homeostasis for the avoidance of IBD[21,23,53]. Specifically, the administration of ITE prevents low-dose dextran sulfate sodium (DSS)-induced IBD in mice[54,55]. To assess the role of STING1 in affecting AHR activation and function *in vivo*, we orally treated WT and *Sting1*$^{Gt/Gt}$ mice with low-dose DSS in the presence of vehicle or ITE (Fig. 6A). DSS treatment caused shortening of colons (a sign of inflammation) and increased myeloperoxidase activity (biomarker of oxidative damage) in WT and *Sting1*$^{Gt/Gt}$ mice to a similar level, indicating that STING1 by itself does not affect the pathogenesis of moderate IBD (Fig. 6B, 6C, and S6A). In sharp contrast, ITE administration improved colon length and reduced myeloperoxidase activity in WT, but not in *Sting1*$^{Gt/Gt}$ mice (Fig. 6B, 6C, and S6A).

In WT and *Sting1*$^{Gt/Gt}$ mice, DSS induced IBD-related histological changes, such as crypt architecture disarray, mucin and goblet cell depletion, epithelial erosion and ulceration, and widening of the gap between the base of the crypt and muscularis with deep mucosal lymphocytosis[56] (Fig. 6D). The protective effect of ITE against DSS-induced histological changes in colon tissue was observed in WT, but not in *Sting1*$^{Gt/Gt}$ mice (Fig. 6D). Inactivation of STING1 also abolished the ITE-regulated production of *Tnf*, *Il6, Il17a* (interleukin 17A), and *Il22* (interleukin 22), while it did not affect the production of *Il23a* (interleukin 23 subunit alpha) or *Il23r* (interleukin 23 receptor) (Fig. 6E, 6F, and S6B). Furthermore, it impaired the activation of type 3 innate lymphoid cells (ILC3) and Th17 subsets, which are known to be induced by AHR activation and produce the anti-inflammatory cytokine IL22 for protection against IBD (Fig. 6G and 6H)[55]. Thus, STING1 is indispensable for the anti-inflammatory effect of the AHR ligand ITE.

To further identify the AHR and STING1-mediated signaling pathways involved in IBD, we investigated the colonic transcriptomes from DSS-treated WT and *Sting1*$^{Gt/Gt}$ mice.

Heatmap analysis of the AHR pathway (WP2586) revealed that a series of AHR downstream genes, including *CYP1A1* and *CYP1B1*, were induced in WT mice, but less so in *Sting1*$^{Gt/Gt}$ mice (Fig. S6C). Pathway enrichment analysis of differentially expressed genes revealed that, in WT mice, ITE administration reversed the inhibition of metabolic pathways by DSS as well as the increase of inflammatory pathways by DSS (Fig. 6I, 6J, and S6D–S6G). In the *Sting1*$^{Gt/Gt}$ group, ITE had minor effects on these pathways. In the context of functional STING deficiency, DSS failed to induce mRNAs coding for type I and type II IFNs and ITE actually further reduced these responses (Fig. 6I, 6J, and S6D–S6G), consistent with the inhibitory effect of ITE on IFN production (Fig. 3C, 3G, and S3B). As a control, DSS activated cytosolic DNA sensing pathways in WT mice, but not in *Sting1*$^{Gt/Gt}$ mice, suggesting a context-dependent pro-inflammatory role of STING1 in IBD.

STING1 is required for AHR-mediated restoration of gut microbial homeostasis

Perturbation of the host-microbiota crosstalk may be an initiator or enhancer of IBD pathogenesis[57]. Although bacterial tryptophan metabolites can protect against IBD through the AHR pathway[58], it is not well understood whether AHR activation improves the gut microbiota during IBD. We thus investigated the impact of AHR and STING1 on the microbiota by performing *16S* ribosomal RNA sequence analysis of fecal samples. DSS treatment reduced the alpha diversity analysis of the microbiota, inhibited *Firmicutes*, and induced *Proteobacteria* in WT and *Sting1*$^{Gt/Gt}$ mice (Fig. 7A and 7B), which is consistent with typical microbial changes during IBD[57,59]. However, ITE administration only reversed these changes in WT, not in *Sting1*$^{Gt/Gt}$ mice. Further cladogram tree and heat map analysis demonstrated that DSS treatment inhibited commensal bacteria (e.g., *Lactobacillus*) and induced pathobionts such as *Helicobacter* in both WT and *Sting1*$^{Gt/Gt}$ mice (Fig. 7C, 7D, 7E, S7A, and S7B). These shifts were largely avoided by ITE treatment in WT, but not *Sting1*$^{Gt/Gt}$ hosts. Thus, STING1 contributes to AHR-mediated microbial regulation, particularly on *Lactobacillus* and *Helicobacter.*

To characterize the changes in the microbiota associated host-microbiota crosstalk, the potential function of gut microbiota was analyzed by using Phylogenetic Investigation of Communities by Reconstruction of Unobserved States (PICRUSt). According to metabolism analysis, ITE regulated microbiota changes associated with energy metabolism in WT mice, but not *Sting1*$^{Gt/Gt}$ mice (Fig. 7F), further confirming that AHR-mediated microbial regulation engages STING1. Kyoto Encyclopedia of Genes and Genomes (KEGG) pathways analysis revealed that DSS treatment-caused microbial changes were strongly associated with lipid metabolism (including phosphonate and phosphinate metabolism, glycosphingolipid biosynthesis, and sphingolipid metabolism) in both WT and *Sting1*$^{Gt/Gt}$ mice (Fig. 7G). In WT mice, ITE-induced microbiota changes were associated with bile acid biosynthesis, a key class of microbiota-associated metabolites during IBD[60,61], and such ITE-elicited changes were absent in *Sting1*$^{Gt/Gt}$ mice.

Collectively, these results indicate that STING1 is involved in the AHR-dependent restoration of a metabolically healthy gut microbiota.

DISCUSSION

The microbiota can regulate and train the host immune system. In turn, the immune system is critical for maintaining the host's microbial diversity[62]. In this study, we establish a direct molecular link between STING1 and AHR, which are key regulators of innate immunity and gut microbiota homeostasis, respectively. Our findings nuclear STING1's role as an adapter protein stimulating AHR-dependent gene transcription independently of classical CGAS-mediated STING1 activation. Phenotypically, STING1 is critical for maintaining AHR-dependent gut eubiosis and dampening proinflammatory signals leading to IBD.

STING1 acts as a multi-functional adaptor in regulating immune-dependent and -independent functions according to its subcellular localizations on different organelles[19]. In the resting state, STING1 locates on the ER and binds to other ER proteins, thus regulating calcium (Ca^{2+}) signaling[29], ER stress[63], and cell death pathways[28]. STING1 can interact with the ER Ca^{2+} channel ITPR1 (inositol 1,4,5-trisphosphate receptor type 1) to control Ca^{2+} release from the ER to the cytoplasm and subsequent inflammatory pyroptosis[29]. Upon activation of the canonical CGAS-STING1 pathway, STING1 exits the ER and is transported to the ERGIC and Golgi apparatus, where it activates type I IFN production or initiates a cellular degradation process, autophagy[16,17]. As a common consequence, STING1 is degraded in the lysosomes, where it also triggers lysosome-dependent cell death[17,64,65]. In addition, STING1 can relocalize to mitochondria as an immune adapter for the detection of RNA viruses or mitochondrial DNA[66,67]. In addition to its functions in cytoplasmic organelles, a nuclear location of STING1 has been reported[50,68], but its function and modulation remains incompletely understood. STING1 trafficking in different subcellular compartments is regulated by multiple pathways, such as COPI (coat protein complex I)-, COPII (coat protein complex II)-, clathrin-coated vesicles, ESCRT (endosomal sorting complexes required for transport)-dependent autophagy, and the microtubule cytoskeleton[17,69–71]. Similar to previous studies[35,68,72], we observed the redistribution of STING1 to the nuclear envelope upon AHR activation. Understanding the role of STING1 in different cellular locations is crucial for defining its multifaceted functions in inflammation and immunity.

In this study, we unveil a nuclear role for STING1 in mediating AHR activation independent of the known ARNT pathway. We identified three STING1-binding proteins, including positive regulators (PML) and negative regulators (DHX9 and XRCC6), which apparently form a large nucleoprotein complex to fine-tune the transcriptional activity of AHR. In short, PML acts as a co-transcriptional factor of AHR, whereas DHX9 and XRCC6 serve as negative regulators of AHR activation partly by favoring its degradation. Our findings suggest that the nuclear transcription machinery of AHR has both accelerating and braking elements/proteins, delineating a tentative strategy for controlling AHR activation. Regardless, the putative role of additional nuclear STING1-binding proteins in controlling AHR activation requires further scrutiny[35,73].

We postulate an antagonistic relationship between nuclear and cytoplasmic STING1. Nuclear translocation of STING1 restricts the activation of the cytoplasmic CGAS-STING1 pathway leading to type I IFN production, whereas the sequestration of STING1 at the

ERGIC can limit the availability of STING1 for stimulating AHR function in the nucleus. This position-dependent polarized relationship may also reflect the duality and saturation of STING1 in the regulation of inflammatory responses. A similar phenomenon is observed with nuclear CGAS, which can interact with nucleosomes or chromatin to influence gene expression rather than immune responses[74]. To maintain the full range of STING1 functions in different organelles, it may be necessary to increase *STING1* gene transcription or prevent its protein degradation. The CBD domain of STING1 can form a ligand-binding pocket and contains multiple post-translational modification sites[73,75]. Although we demonstrated that the CBD domain of STING1 binds the N-terminal domain of AHR to control AHR transcriptional activity, the exact mechanism of STING1 nuclear translocation remains unclear. It is well-established that tryptophan plays a role in anchoring membrane proteins and dealing with hydrophobic mismatches at the lipid–water interface[76]. Additionally, ER-generated lipid droplets can potentially move into the nucleoplasm, as well as the inner nuclear membrane, due to their interaction with PML on their surface[77]. Given the discovery in this study that AHR ligands and PML bind with STING1 in the nucleus, an unexplored possibility arises: AHR ligands may directly prompt the translocation of STING1 to the nucleus through interactions with ER-associated membrane lipid dynamics facilitated by PML binding[35,72,78].

IBD is a highly prevalent condition featuring chronic inflammation, intestinal barrier dysfunction, and microbial disturbance[79–81]. STING1 plays an ambiguous pro- or anti-inflammatory role in IBD pathogenesis, depending on the experimental models[27,82–85]. STING1 can engage AHR to mediate IL10 expression or inhibit RORγt-mediated IL17 expression in Th17 cells, independent of type I IFNs[86]. We calibrated the system in a way that low-dose DSS-induced moderate colitis resulted in typical inflammatory responses, intestinal damage, and dysbiosis that were indistinguishable in WT and *Sting1*$^{Gt/Gt}$ mice. AHR plays multiple beneficial roles in various cell types in defense against IBD. In immune cells, particularly ILC3s and Th17 cells, AHR ligands promote IL17 and IL22 production[55,87,88], which helps suppress inflammation and mitigate intestinal epithelial damage. Our results revealed that ITE promoted DSS-induced accumulation of ILC3 and Th17 cells in colon tissues, while the loss of *Sting1* inhibited ITE-mediated induction of ILC3 and Th17 cells.

In intestinal epithelial cells, AHR activation is important for regulating metabolic clearance and stem cell differentiation[89], which are essential for intestinal barrier integrity and epithelial function. We also observed that AHR activation in the intestinal environment improved metabolism, reduced inflammation, and restored the barrier in IBD, dependent on STING1. Thus, the loss of STING1 disrupted the AHR-mediated anti-inflammatory effects in multiple ways.

Although the inter-regulatory mechanisms between inflammation and microbiota changes remain largely unknown[90], fecal microbiome analysis suggest that STING1 is important for AHR-mediated microbial regulation. DSS induced typical dysbiosis, including decreased microbiota diversity, reduced *Firmicutes*, and enhanced *Proteobacteria*, whereas AHR activation reversed these changes in a STING1-dependent manner. Among *Firmicutes*, commensal bacteria *Lactobacillaceae* (e.g., *Lactobacillus gasseri, Lactobacillus jensenii,*

and *Lactobacillus reuteri*) were mostly reduced upon DSS treatment and then restored by AHR activation, which is consistent with the observation that *Lactobacilli* could produce tryptophan metabolites and reduce colitis in an AHR-dependent manner[91,92]. In contrast, among *Proteobacteria*, harmful bacteria from the *Helicobacter* genus (e.g., *Helicobacter typhlonius, Helicobacter hepaticus,* and *Helicobacter ganmani*) were mostly increased by DSS and reduced by AHR activation. Although *Helicobacter pylori* infection has been associated with DSS-induced ulcerative colitis and AHR is involved in *Helicobacter pylori*-related gastric pathogenesis[93,94], the role of AHR in suppressing *Helicobacter* infection during IBD appears novel. Furthermore, the STING1-dependent ITE-mediated favorable effects on the gut microbiota were associated with energy metabolism and bile acid biosynthesis, consistent with previous studies[58,95].

In summary, we demonstrated a non-canonical role for nuclear STING1 in promoting AHR activation through transcriptional mechanisms. Our discovery that STING1 drives AHR-mediated gut homeostasis at the microbial and immunological levels may establish a novel strategy to combat IBD.

Limitations of the study

Our study highlights the role of nucleus-localized STING1 in promoting AHR function, tissue repair, and the regulation of dysbiosis in the context of DSS-mediated colitis. However, the exact mechanism responsible for STING1 translocating into the nucleus remains unclear and requires further investigation. Additionally, while we have confirmed the necessity of STING1 for AHR-regulated IL22 production in ILC3 and Th17 cells, and have identified the adverse effects of STING1 deletion on Th17 cell activation, the specific cell types that rely on the STING1-AHR axis for protection against gut inflammation and maintenance of homeostasis warrant further investigation in future studies.

STAR Methods

RESOURCE AVAILABILITY

Lead contact—Further information and requests for resources and reagents should be directed to and will be fulfilled by the lead contact, Daolin Tang (daolin.tang@utsouthwestern.edu).

Materials availability—The plasmids and cell lines generated in this study are available from the lead contact upon request.

Data and code availability

- The next-generation sequencing data and 16S rRNA gene sequencing data have been deposited at NCBI Sequence Read Archive (SRA) and are publicly available as of the date of publication. Accession numbers are listed in the key resources table.
- This paper does not report original code.

- Any additional information required to analyze the data reported in this paper is available from the lead contact upon request.

EXPERIMENTAL MODEL AND STUDY PARTICIPANT DETAILS

Experimental animals—C57BL/6J WT (Cat#000664; RRID:IMSR_JAX:000664) and *Sting1*$^{Gt/Gt}$ (Cat#017537; RRID:IMSR_JAX:017537) mice were purchased from The Jackson Laboratories and maintained in our facilities. *Sting1*$^{Gt/Gt}$ mice carry a missense mutation in exon 6 of the *Sting1* gene resulting in an isoleucine-to-asparagine change at amino acid 199 and no gene product at the protein level[26]. Mice were housed with their littermates in groups of 4 animals per cage and kept on a regular 12-h light and dark cycle (7:00–19:00 light period; room temperature: 20°C-25°C; relative humidity: 40% −60%). Food and water were available ad libitum. Experiments were carried out under pathogen-free conditions, and the health status of mouse lines was routinely checked by veterinary staff. Experiments were carried out with randomly chosen littermates of the same sex and matched by age and body weight. We conducted all animal care and experimentation in accordance with the Association for Assessment and Accreditation of Laboratory Animal Care guidelines (http://www.aaalac.org) and with approval from institutional animal care and use committees (UT Southwestern Medical Center [#102605]).

Six- to 8-week-old WT and *Sting1*$^{Gt/Gt}$ male and female mice were randomly assigned to vehicle, DSS, and DSS+ITE groups for experiments. Colitis was induced in mice from DSS and DSS+ITE groups with two alternate cycles of 2% DSS (MP Biomedicals, 101516; MW 8,000 [avg]) treatment. One cycle consisted of 2% DSS in distilled water for 7 days, followed by a 7-day interval of distilled water. As control, the vehicle mice received distilled water for 28 days. ITE treatment was conducted in mice from DSS+ITE groups, that received intraperitoneal injection of 100 μl ITE (Invivogen, tlrl-ite; 10 mg/kg, body, dissolved in phosphate-buffered saline [PBS]) twice a week for 28 days. As control, mice from vehicle and DSS groups were intraperitoneally injected with 100 μl DMSO vehicle (dissolved in PBS) twice a week for 28 days. At the end of the experimental period, mice were sacrificed, blood was collected, fecal matter was reserved in DNA/RNA Shield (Zymo Research, R1100) and colon samples were washed with PBS, followed by measuring the length, cut longitudinally, and stored.

Cell lines and primary macrophages—THP1 cell lines was cultured in RPMI 1640 supplemented with 10% fetal bovine serum (FBS; Gibco, 25300), 1% penicillin-streptomycin (Gibco, 15070), and 100 μg/ml normocin (InvivoGen, ant-nr-1). HT-29, HT29-Lucia™ AHR cells, HeLa, MEFs, and 293FT cell lines were cultured in high-glucose DMEM supplemented with 10% FBS and 100 units/ml penicillin/streptomycin.

For primary peritoneal macrophages isolation, the indicated C57BL/6 mice were injected with 3% brewer thioglycolate medium (MilliporeSigma, B2551) allowing an inflammatory response to proceed for 4 days. Then, mice were euthanized in a CO_2 chamber and death was confirmed by cervical dislocation. Primary peritoneal macrophages were isolated from peritoneal cavity and seeded on 6-well plates cultured in DMEM/F-12 (Gibco, 11320)

supplemented with 10% FBS and 1% penicillin-streptomycin. Fresh medium was added after 3 h. Nonadherent cells were removed by gently washing three times with warm PBS.

For the *in vitro* differentiation of Th17 cells, we followed a previously described method [96]. Naïve $CD4^+$ T cells were isolated from the spleen tissues of both WT and *Sting1*$^{Gt/Gt}$ mice using a mouse $CD4^+$ T cell isolation kit (Stemcell Technologies, 19765). Subsequently, the naïve $CD4^+$ T cells were activated via T cell receptor (TCR) signaling with plate-bound anti-CD3ε (Invitrogen, 14–0033-82, 2 μg/mL) and anti-CD28 (Invitrogen, 14–0281-82, 2 μg/mL) antibodies. To induce Th17 differentiation, the following reagents were employed: 5 ng/mL recombinant human TGF-β1 (Proteintech, HZ-1011), 40 ng/mL recombinant mouse IL-6 (Miltenyi Biotec, 130–094-065), 20 ng/mL recombinant mouse IL-23 (Miltenyi Biotec, 130–096-676), and 1 μg/mL mouse IFN-γ antibody (R&D Systems, MAB485-SP). The cells were cultured for 108 hours and then collected for RNA analysis and flow cytometry. For flow cytometry analysis, we used mouse IL17A antibody (Abcam, ab79056) and CD4 antibody (BioLegend, 100405) to detect the differentiation of Th17 cells.

All cells were grown at 37°C, 95% humidity, and 5% CO_2 in an incubator. All cell lines used were authenticated using short tandem repeat profiling, and mycoplasma testing was negative.

METHOD DETAILS

RNAi—Predesigned MISSION shRNA bacterial glycerol stocks were purchased from Sigma-Aldrich, and plasmids expressing shRNAs were extracted using a NucleoBond Xtra Midi EF Kit (Macherey-Nagel, 740410) according to the manufacturers' instructions. To achieve stable knockdown in THP1 cells, shRNA plasmids targeting the indicated genes, together with two packing plasmids, psPAX2 (Addgene, 12260; deposited by Didier Trono) and pMD2.G (Adggene, 12259; deposited by Didier Trono), were first transfected into 293FT cells using Lipofectamine 3000 reagent (Invitrogen, L3000). Supernatants containing shRNA-expressing lentivirus were collected 48 h after transfection and then used to infect the indicated cells (1×10^6) for another 48 h. Positive cells were selected in culture medium with appropriate dose of puromycin (3–5 μg/ml) according to cell types. The efficiency of gene knockdown was tested by western blot analysis using the corresponding antibodies. The sequence or order of information of shRNA is shown in Table S2.

Plasmid construction and transfection—A STING1 expression plasmid (RC208418) was purchased form OriGene, and a PML expression plasmid (370640210600) was obtained from Applied Biological Materials. The AHR expression plasmid was created by the Tang Lab. Briefly, the cDNA from the human *AHR* gene was cloned from mRNA of THP1 cells by PCR into the HindIII sites of the pCDNA3.1 vector (Addgene, 128023; deposited by Oskar Laur). The mutations in the *STING1* or *AHR* genes were introduced using a Q5 Site-Directed Mutagenesis Kit (New England Biolabs, E0554S). All plasmids were confirmed by DNA sequencing.

For THP1 cell transfection, cells (2×10^6/ml) were seeded in 6-well plates and a total of 5 μg expression plasmids or corresponding mutant plasmids were transfected by electroporation

using the Neon Transfection System (Thermo Fisher Scientific, MPK5000) with parameters of 1400 V, 20 ms, and 2 pulses.

For HT-29, MEFs, and 293FT cells transfection, the plasmids were transfected into cells (1×10^6/ml) using Lipofectamine 3000 reagent (Invitrogen, L3000) according to the manufacturer's instructions. The efficiency of gene transfection was then tested by western blot analysis.

RNA isolation and qPCR—Total RNA was isolated from cultured cells using the E.Z.N.A. HP Total RNA Kit (Omega Bio Tek, 6812–01) according to the manufacturer's instructions. RNA concentrations were measured with the Nanodrop One Spectrophotometer (Thermo Fisher Scientific, 13–400-525). cDNA was amplified from total RNA using a PrimeScript RT Reagent Kit (Takara, RR037A) according to the manufacturer's instructions. Individual 20 μl real-time PCR reactions consisted of 20 μl of SYBR Green qPCR Master Mix (Bimake, 21203), 8 μl of diluted cDNA, and 1 μl of each 10 μM forward and reverse primer. qPCR analysis was performed using a CFX96 Touch Real-Time PCR Detection System (Bio-Rad, CFX96). The sequence of all primers are listed in Table S3.

Cell viability assay—THP1 or MEF cells were seeded at 1×10^4 cells/well into 96-well plates and incubated in 100 μl of fresh medium with the indicated drugs for 24 h. Subsequently, 10 μl of Cell Counting Kit-8 (Bimake, B34302) solution was added to the cells and incubated for 1 h in an incubator of 5% CO_2 at 37°C. The absorbance at 450 nm was measured using a Cytation 5 microplate reader (BioTek).

Luciferase assay—The indicated HT29-Lucia AHR cells (5×10^5/ml) were cultured in 96-well plates overnight and then treated with AHR ligands for 16–24 h for each condition in triplicate. In experiments with STING1 mutants, ITE was added to the medium 6 h after transfection of the mutants. The luciferase activity was measured with or without drug treatment using a QUANTI-Luc Luciferase Detection Kit (InvivoGene, rep-qlcg1) according to the manufacturer's protocol. Luminescence was measured using a Cytation 5 microplate reader.

Immunofluorescence assay—For HT-29 and HeLa staining, cells (1×10^5/ml) were placed in each well of a 24-well plate with coverslips at the bottom. For THP1 staining, cells (8×10^4/ml) were suspended in PBS and centrifuged onto the slides using a Cytospin 4 Cytocentrifuge (Thermo Fisher Scientific). After transfection or drug treatment for the indicated times, cells on the coverslips or slides were fixed with 4% paraformaldehyde (Thermo Fisher Scientific, J19943.K2) for 15 min at room temperature, permeabilized with 0.3% Triton X-100 (Sigma, 9002–93-1) for 15 min at room temperature, blocked with 2% BSA (Gemini, 700–105P) for 1 h at room temperature, and incubated with the indicated primary antibodies against AHR (Santa Cruz Biotechnology, sc-133088; 1:50); LMAN1 (Santa Cruz Biotechnology, sc-365158; 1:50); PML (Santa Cruz Biotechnology, sc-966; 1:50), and FLAG (Cell Signaling Technology, 14793; 1:200) at 4°C overnight. Fluorescent dye-labeled secondary antibodies Alexa Fluor 488 anti-mouse (Thermo Fisher Scientific, A32723; 1:200) and Alexa Fluor 555 anti-rabbit (Thermo Fisher Scientific, A21428; 1:200)

were incubated with cells protected from light for 1 h at room temperature, and then stained with DAPI (MilliporeSigma, MBD0015) for 5 min.

For colon tissues, the samples were fixed in 10% formalin for 48 h and subsequently processed and embedded at the Histo Pathology Core at UT Southwestern Medical Center. To perform antigen retrieval, the slides were heated at 95°C in 10 mM sodium citrate for 20 min. For cells on coverslips or slides, they were fixed with 4% paraformaldehyde (Thermo Fisher Scientific, J19943.K2) for 15 min at room temperature, followed by permeabilization with 0.3% Triton X-100 (Sigma, 9002–93-1) for 15 min at room temperature. Blocking was performed with 2% BSA (Gemini, 700–105P) for 1 h at room temperature. The cells were then incubated overnight at 4°C with the appropriate primary antibodies, including CD3 (Santa Cruz Biotechnology, sc-20047; 1:50), IL17A (Abcam, ab79056; 1:200), and ROR gamma (t)/RORγt (Thermo Fisher Scientific, 46–6981-82; 1:200). For fluorescent detection, the cells were incubated with fluorescent dye-labeled secondary antibodies, such as Alexa Fluor 594 anti-mouse (Thermo Fisher Scientific, A11005; 1:200) and Alexa Fluor 488 anti-rabbit (Thermo Fisher Scientific, A11008; 1:200), for 1 h at room temperature, protected from light. Finally, the cells were stained with DAPI (MilliporeSigma, MBD0015) for 5 min. Coverslips or slides were covered with Fluoromount-G (Electron Microscopy Sciences, 17984–25) and images were visualized with a confocal microscope (Nikon). Images were analyzed and reconstructed using the Z-stack function in NIS-element software to generate 3D models.

Cell fractionation assay—THP1 (1×10^6/ml) cells were cultured in Petri dishes and then treated with AHR ligands for the indicated times. The cell fractionation assay was conducted using a Cell Fractionation Kit (Cell Signaling Technology, 9038) according to the manufacturer's protocol followed by immunoblot or immunoprecipitation analysis.

Immunoblot and immunoprecipitation assay—Cells were lysed in cell lysis buffer A (20 mM Tris-HCl, pH 6.8, 25 mM NaCl, 10% glycerol, 0.2% SDS, and 0.5 mM EDTA) supplemented with a phosphatase and protease inhibitor cocktail (Thermo Fisher Scientific, 78430) for 30 min on ice followed by centrifugation at 14,000 g for 15 min at 4°C. For non-reducing sodium dodecyl sulfate-polyacrylamide gel electrophoresis (SDS-PAGE), cells were lysed in cell lysis buffer B (20 mM HEPES, pH 7.0, 25 mM NaCl, and 10% glycerol) supplemented with the phosphatase and protease inhibitor cocktail for 30 min on ice followed by centrifugation at 14,000 g for 15 min at 4°C. Blue native page was conducted as described previously [8]. Protein concentrations were determined using a BCA Protein Assay Kit (Thermo Fisher Scientific, 23225). Proteins were separated on 4%–12% precast polyacrylamide gels (Bio-Rad, 3450126) in XT MES running buffer (Bio-Rad, 3450126) and then transferred onto polyvinylidene difluoride membranes (Bio-Rad, 1610789). The membranes were blocked with 5% non-fat milk (Research Products International, M17200) in PBS-Tween (PBST, MilliporeSigma, P3563) for 1 h at room temperature, incubated with primary antibodies against STING1 (Cell Signaling Technology, 13647 or 50494; 1:1000), AHR (Cell Signaling Technology, 83200; 1:1000), MAP1LC3/LC3 (Cell Signaling Technology, 12741; 1:1000), ATG5 (Cell Signaling Technology, 12994; 1:1000), SQSTM1 (sequestosome 1) (Cell Signaling

Technology, 23214; 1:1000), p-IRF3 (Cell Signaling Technology, 37829; 1:1000), p-STING1 (Cell Signaling Technology, 19781; 1:1000), IRF3 (Cell Signaling Technology, 4302; 1:1000), p-TBK1 (Cell Signaling Technology, 5483; 1:1000), CGAS (Cell Signaling Technology, 31659; 1:1000), HSP90 (Cell Signaling Technology, 4877; 1:1000), COX4I1/COX4 (cytochrome C oxidase subunit 4I1) (Cell Signaling Technology, 4844; 1:1000), MT-CO2/COX2 (mitochondrially encoded cytochrome C oxidase II) (Cell Signaling Technology, 4842; 1:1000), H3C1/Histone H3 (H3 clustered histone 1) (Cell Signaling Technology, 9715; 1:1000), ARNT (Santa Cruz Biotechnology, sc-55526; 1:200), DHX9 (Santa Cruz Biotechnology, sc-137232; 1:200), XRCC6 (Santa Cruz Biotechnology, sc-17789; 1:200), RNF20 (Santa Cruz Biotechnology, sc-517358; 1:200), PML (Santa Cruz Biotechnology, sc-966; 1:200), FLAG (Cell Signaling Technology, 14793; 1:1000), HA (Cell Signaling Technology, 3724; 1:1000), HIS (Cell Signaling Technology, 2365; 1:1000), GAPDH (glyceraldehyde-3-phosphate dehydrogenase) (Cell Signaling Technology, 2118; 1:6000), and/or ACTB (actin beta) (Cell Signaling Technology, 3700; 1:6000) overnight at 4°C. After the incubation with a horseradish peroxidase (HRP)-linked anti-mouse immunoglobulin G (IgG) secondary antibody (Cell Signaling Technology, 7076; 1:5000) or HRP-linked anti-rabbit IgG secondary antibody (Cell Signaling Technology, 7074; 1:5000) for 1 h at room temperature, the membranes were visualized and analyzed with a ChemiDoc Touch Imaging System (Bio-Rad). The intensities of bands were analyzed with Image Lab software.

For immunoprecipitation, cells were lysed in IP Lysis Buffer (25 mM Tris-HCl, pH 7.5, 150 mM NaCl, 15% glycerol, 1% NP40, and 0.5 mM EDTA) supplemented with the phosphatase and protease inhibitor cocktail for 30 min on ice followed by centrifugation at maximum speed for 15 min at 4°C. Supernatants were collected and protein concentrations were measured with a BCA Protein Assay Kit (Thermo Fisher Scientific, 23225). Proteins (500 μg) were precleared with Protein A Magnetic Beads (Millipore, LSKMAGA10) at room temperature for 20 min. Then supernatants were collected and incubated with mouse IgG control (Cell Signaling Technology, 5415; 1:500), anti-HA antibody (Cell Signaling Technology, 3724, 1:50), anti-AHR antibody (Santa Cruz Biotechnology, sc-133088, 1:20), or anti-STING1 antibody (Cell Signaling Technology, 50494, 1:50) overnight at 4°C with continuous rotation mixing. Protein A Magnetic Beads were suspended and washed with PBST 3 times, and then incubated with pre-formed protein-antibody complex for 10 min at room temperature. Precipitated proteins were eluted by boiling in 4×sodium dodecyl sulfate (SDS) sample buffer (Bio-Rad, 1610791) for 5 min, followed by analyzing the supernatant by SDS-PAGE and immunoblotting. For nuclear immunoprecipitation, cells were lysed as described in the cell fractionation assay method and the nuclear component was used to perform immunoprecipitation in IP Lysis Buffer.

Protein docking—For protein-drug docking, the structures of STING1 (PDB: 6NT5), 2’3’-cGAMP (PubChem CID: 145712307), ITE (PubChem CID: 4668801), and L-KYN (PubChem CID: 161166) were employed in the protein-protein docking analysis conducted with CB-Dock [97]. Molecular graphics were generated using PyMOL.

For the protein-protein docking, the human structures of STING1 (AlphaFold2: AF-Q86WV6) and AHR (AlphaFold2: AF-P35869) were chosen for the protein-protein docking analysis. The docking protocol used was based on the method described by de Vries et

al.[98]. Specifically, the contact region for AHR was defined as residues 1–400, while no restrictions were placed on STING1. The ideal binding mode was determined based on biological insights and ranking scores. The final structure obtained after molecular dynamics simulation was analyzed using the PISA interface server (https://www.ebi.ac.uk/pdbe/pisa/). Molecular graphics were generated using PyMOL.

CETSA in cellular lysates—THP1 cells were cultured at a density of 1×10^6 cells/mL and treated with either 15 μM ITE (InvivoGen, tlrl-ite), 10 μg/mL 2'3'-cGAMP (InvivoGen, tlrl-nacga23), or DMSO for 1 hour. Subsequently, cells were collected in PBS buffer (pH 7.4) to which a protease inhibitor cocktail (Thermo Fisher Scientific, 78430) was added. The cell suspensions were then aliquoted into PCR tubes (50 μL volume, approximately 1 million cells per condition) and heated at different temperatures (ranging from 40°C to 82°C in 3°C increments) in a thermocycler for 3 minutes, followed by cooling to room temperature for an additional 3 minutes. NP40 was introduced to the suspensions to reach a final concentration of 0.2% (v/v), and the suspensions were thoroughly mixed. Cell lysis was achieved through three freeze-thaw cycles in liquid nitrogen, followed by incubation on ice with occasional vortexing for 20 minutes. After lysis, the lysates were centrifuged at 15,000 g (4°C) for 20 minutes to remove insoluble material. Finally, the samples were diluted with SDS loading buffer for western blotting analysis.

Liquid chromatography-mass spectrometry (LC-MS) assay—The LC-MS was performed by the Proteomics Core Lab of UT Southwestern Medical Center according to the following method: Protein gel pieces were reduced and alkylated with DTT (20 mM) and iodoacetamide (27.5 mM). A 0.1 μg/μl solution of trypsin in 50 mM triethylammonium bicarbonate/TEAB was added to completely cover the gel, allowed to sit on ice, and then 50 μL of 50 mM triethylammonium bicarbonate was added and the gel pieces were digested overnight. Following solid-phase extraction cleanup with an Oasis MCX μelution plate (Waters), the resulting peptides were reconstituted in 10 μl of 2% (v:v) acetonitrile (ACN) and 0.1% trifluoroacetic acid in water. Two μl of this were injected onto an Orbitrap Elite mass spectrometer (Thermo Electron) coupled to an Ultimate 3000 RSLC-Nano liquid chromatography systems (Dionex). Samples were injected onto a 75 μm ID * 15 cm long EasySpray column (Thermo), and eluted with a gradient from 0–28% buffer B over 60 min. Buffer A contained 2% (v:v) ACN and 0.1% formic acid in water, and buffer B contained 80% (v:v) ACN, 10% (v:v) trifluoroethanol, and 0.1% formic acid in water. The mass spectrometer operated in positive ion mode. MS scans were acquired at 240,000 resolutions in the Orbitrap and up to 14 MS/MS spectra were obtained in the ion trap for each full spectrum acquired using collisionally induced dissociation/CID. Dynamic exclusion was set for 15 s after an ion was selected for fragmentation. Raw MS data files were analyzed using Proteome Discoverer v2.2 (Thermo), with peptide identification performed using Sequest HT searching against the human protein database from UniProt. Fragment and precursor tolerances of 10 ppm and 0.6 Da were specified, and three missed cleavages were allowed. Carbamidomethylation of Cys was set as a fixed modification, with oxidation of Met set as a variable modification. The false-discovery rate (FDR) cutoff was 1% for all peptides.

Histopathological examinations—The colon tissues were fixed in 10% formalin for 48 h. The fixed tissues were submitted to the Histo Pathology Core at UT Southwestern Medical Center for processing, embedding, and hematoxylin and eosin/H&E staining; the images were captured by the EVOS imaging system (Thermo Fisher Scientific).

Enzyme-linked immunosorbent assay (ELISA)—Serum TNF and IL6 concentrations were detected using the TNF ELISA Kit (BioLegend, 430907) and the IL6 ELISA Kit (BioLegend, 4313075) following the manufacturer's instructions.

Next-generation sequencing—The next-generation sequencing was performed by the Sequencing Core Lab of UTSW according to the following method: The Agilent 2100 Bioanalyzer system and the RNA Nano chip kit (Agilent, 5067–1511) were used for RNA quality measurement. An Illumina TruSeq® Stranded mRNA Library prep kit (Illumina, 20020594) was used to generate the RNA libraries. The first step in the workflow involves purifying the polyA-containing mRNA molecules using oligo-dT-attached magnetic beads. Following purification, the mRNA is fragmented into small pieces using divalent cations under elevated temperature. The cleaved RNA fragments are copied into first-strand cDNA using reverse transcriptase and random primers. Second-strand cDNA synthesis follows, using DNA polymerase I and RNase H. The cDNA fragments then go through an end repair process, the addition of a single 'A' base, and then ligation of the adapters. The products are then purified and enriched with PCR to create the final cDNA library. The total RNA input amount per each sample was 2 μg; 94°C for 5 min was used for mRNA fragmentation; the UMI adapters synthesized by IDT (Integrated DNA Technology) were used in the ligation step; followed by two times of AMPure XP beads (Beckman Coulter, A63881) purification, and then PCR amplification using 10 cycles to generate the final cDNA libraries. Again, AMPure XP beads purifications were performed two times before the assessment took place. The library quantity was measured using the picogreen method; the Quant-iT™ PicoGreen dsDNA Assay kit by (Invitrogen, P7589) and PerkinElmer plate reader (PerkinElmer Victor X3, 2030 Multilabel Reader) were used in the assessment. The library quality was verified on an Agilent 2100 Bioanalyzer instrument using the Agilent DNA 1000 kit (Agilent Technologies, 5067–1504). All libraries must meet the QC requirements before they were moved forward for sequencing. Sample were sequenced on an Illumina NovaSeq 6000 sequencer platform with S4 flowcell and XP workflow PE-150. For primary data analysis, adapter trimming and quality trimming were performed with trimgalore (v0.6.4), and ribosomal RNA was removed using SortMeRNA (v2.1b). Trimmed and filtered reads were aligned to reference (GRCh37) with STAR (vSTAR2.6.1d). FeatureCounts (v1.6.4) was used for gene counts, biotype counts, and rRNA estimation. FPKMs for genes and transcripts were generated by StringTie (v2.0), and RSeQC (v3.0.1) was used for generating RNA quality control metrics.

***16S* rRNA gene sequencing on the MinION platform—**For amplification of the V1-V9 region of the *16S* rRNA gene, the following inner primers were used, with *16S* rRNA gene-specific sequences underlined: forward primer (S-D-Bact-0008-c-S-20 [99] with anchor sequence 5'-TTTCTGTTGGTGCTGATATTGCAGRGTTYGATYMTGGCTCAG-3' and reverse primer (1492R) with anchor sequence 5'-

ACTTGCCTGTCGCTCTATCTTCCGGYTACCTTGTTACGACTT-3'. PCR amplification of *16S* rRNA genes was conducted using the KAPA2G™ Robust HotStart ReadyMix PCR Kit (Kapa Biosystems, Wilmington, MA, USA) in a total volume of 25 µl containing inner primer pairs (50 nM each) and the barcoded outer primer mixture (3%) from the PCR Barcoding Kit (Oxford Nanopore Technologies, SQK-PBK004). Amplification was performed with the following PCR conditions: initial denaturation at 95°C for 3 min, 5 cycles of 95°C for 15 s, 55°C for 15 s, and 72°C for 30 s, 30 cycles of 95°C for 15 s, 62°C for 15 s, and 72°C for 30 s, followed by a final extension at 72°C for 1 min. Amplified DNA was purified using AMPure® XP and quantified with a NanoDrop® 1000 (Thermo Fischer Scientific). A total of 100 ng of DNA was incubated with 1 µl of Rapid Adapter at room temperature for 5 min. The prepared DNA library (11 µl) was mixed with 34 µl of Sequencing Buffer, 25.5 µl of Loading Beads, and 4.5 µl of water, loaded onto the R9.4 flow cell (Oxford Nanopore Technologies, FLO-MIN106), and sequenced on the MinION™ Mk1B. MINKNOW software ver. 1.11.5 (Oxford Nanopore Technologies) was used for data acquisition. Albacore software ver. 2.3.4 (Oxford Nanopore Technologies) was used for basecalling the MinION™ sequencing data (FAST5 files) to generate pass reads (FASTQ format) with a mean quality score > 7. The adapter and barcode sequences were trimmed using the EPI2ME Fastq Barcoding workflow ver. 3.10.4 (Oxford Nanopore Technologies). The reads were filtered in operational taxonomic unit (OTU) groups by using TaxonKit software, based on the size distribution of *16S* rRNA gene sequences in the Greengene database[100].

Bioinformatics analysis—For bioinformatics analysis of LC-MS data, Gene ontology (GO) analysis of nuclear STING1-binding proteins was performed by the web server g:Profiler[101].

For bioinformatics analysis of NGS data, differential gene expression profiles and gene ontology biological process terms enrichment were generated by the web server iDEP[102]. Hallmark pathway, Wiki pathway, and KEGG pathway enrichment analysis were performed by gene set enrichment analysis (GSEA). Software for utilizing GSEA is available from the Broad Institute[103]. Enrichment score/ES reflects the degree to which a gene set is over-represented in our dataset of differentially expressed genes. Normalized enrichment score/NES is the enrichment score normalized for gene set size.

For bioinformatics analysis of *16S* rRNA gene sequencing data, the abundance and predicted function analysis of microbiota was performed using the MicrobiomeAnalyst software[104]. The linear discriminant analysis effect size (LEfSe) and phylogenetic investigation of communities by reconstruction of unobserved states (PICRUSt) were performed by using ImageGP software[105,106].

QUANTIFICATION AND STATISTICAL ANALYSIS

Data are presented as mean ± SD of three independent experiments except where otherwise indicated. All data met the assumptions of the tests (e.g., normal distribution). Unpaired Student's t tests were used to compare the means of two groups. One-way or two-way analysis of variance (ANOVA) was used for comparison among the different groups. A

two-tailed p value of <0.05 was considered statistically significant. The exact value of n within the figures is indicated in the figure legends. Statistical analyses were performed using GraphPad Prism 9 software.

Supplementary Material

Refer to Web version on PubMed Central for supplementary material.

ACKNOWLEDGMENTS

Research by D.T. and R.K. was supported by grants from the National Institutes of Health (R01CA160417, R01CA229275, R01CA211070, and R01GM127791), and D.J.K. was supported by NIH grant GM131919.

REFERENCES

1. Ishikawa H, and Barber GN (2008). STING is an endoplasmic reticulum adaptor that facilitates innate immune signalling. Nature 455, 674–678. 10.1038/nature07317. [PubMed: 18724357]
2. Ishikawa H, Ma Z, and Barber GN (2009). STING regulates intracellular DNA-mediated, type I interferon-dependent innate immunity. Nature 461, 788–792. 10.1038/nature08476. [PubMed: 19776740]
3. Sun W, Li Y, Chen L, Chen H, You F, Zhou X, Zhou Y, Zhai Z, Chen D, and Jiang Z (2009). ERIS, an endoplasmic reticulum IFN stimulator, activates innate immune signaling through dimerization. Proc Natl Acad Sci U S A 106, 8653–8658. 10.1073/pnas.0900850106. [PubMed: 19433799]
4. Zhong B, Yang Y, Li S, Wang YY, Li Y, Diao F, Lei C, He X, Zhang L, Tien P, and Shu HB (2008). The adaptor protein MITA links virus-sensing receptors to IRF3 transcription factor activation. Immunity 29, 538–550. 10.1016/j.immuni.2008.09.003. [PubMed: 18818105]
5. Sun L, Wu J, Du F, Chen X, and Chen ZJ (2013). Cyclic GMP-AMP synthase is a cytosolic DNA sensor that activates the type I interferon pathway. Science 339, 786–791. 10.1126/science.1232458. [PubMed: 23258413]
6. Burdette DL, Monroe KM, Sotelo-Troha K, Iwig JS, Eckert B, Hyodo M, Hayakawa Y, and Vance RE (2011). STING is a direct innate immune sensor of cyclic di-GMP. Nature 478, 515–518. 10.1038/nature10429. [PubMed: 21947006]
7. Dey B, Dey RJ, Cheung LS, Pokkali S, Guo H, Lee JH, and Bishai WR (2015). A bacterial cyclic dinucleotide activates the cytosolic surveillance pathway and mediates innate resistance to tuberculosis. Nat Med 21, 401–406. 10.1038/nm.3813. [PubMed: 25730264]
8. Ergun SL, Fernandez D, Weiss TM, and Li L (2019). STING Polymer Structure Reveals Mechanisms for Activation, Hyperactivation, and Inhibition. Cell 178, 290–301 e210. 10.1016/j.cell.2019.05.036. [PubMed: 31230712]
9. Zhang BC, Nandakumar R, Reinert LS, Huang J, Laustsen A, Gao ZL, Sun CL, Jensen SB, Troldborg A, Assil S, et al. (2020). STEEP mediates STING ER exit and activation of signaling. Nat Immunol 21, 868–879. 10.1038/s41590-020-0730-5. [PubMed: 32690950]
10. Sun MS, Zhang J, Jiang LQ, Pan YX, Tan JY, Yu F, Guo L, Yin L, Shen C, Shu HB, and Liu Y (2018). TMED2 Potentiates Cellular IFN Responses to DNA Viruses by Reinforcing MITA Dimerization and Facilitating Its Trafficking. Cell Rep 25, 3086–3098 e3083. 10.1016/j.celrep.2018.11.048. [PubMed: 30540941]
11. Dobbs N, Burnaevskiy N, Chen D, Gonugunta VK, Alto NM, and Yan N (2015). STING Activation by Translocation from the ER Is Associated with Infection and Autoinflammatory Disease. Cell Host Microbe 18, 157–168. 10.1016/j.chom.2015.07.001. [PubMed: 26235147]
12. Liu S, Cai X, Wu J, Cong Q, Chen X, Li T, Du F, Ren J, Wu YT, Grishin NV, and Chen ZJ (2015). Phosphorylation of innate immune adaptor proteins MAVS, STING, and TRIF induces IRF3 activation. Science 347, aaa2630. 10.1126/science.aaa2630. [PubMed: 25636800]

13. Zhang C, Shang G, Gui X, Zhang X, Bai XC, and Chen ZJ (2019). Structural basis of STING binding with and phosphorylation by TBK1. Nature 567, 394–398. 10.1038/s41586-019-1000-2. [PubMed: 30842653]
14. Wang Y, Luo J, Alu A, Han X, Wei Y, and Wei X (2020). cGAS-STING pathway in cancer biotherapy. Mol Cancer 19, 136. 10.1186/s12943-020-01247-w. [PubMed: 32887628]
15. Zhang X, Bai XC, and Chen ZJ (2020). Structures and Mechanisms in the cGAS-STING Innate Immunity Pathway. Immunity 53, 43–53. 10.1016/j.immuni.2020.05.013. [PubMed: 32668227]
16. Hopfner KP, and Hornung V (2020). Molecular mechanisms and cellular functions of cGAS-STING signalling. Nat Rev Mol Cell Biol 21, 501–521. 10.1038/s41580-020-0244-x. [PubMed: 32424334]
17. Gui X, Yang H, Li T, Tan X, Shi P, Li M, Du F, and Chen ZJ (2019). Autophagy induction via STING trafficking is a primordial function of the cGAS pathway. Nature 567, 262–266. 10.1038/s41586-019-1006-9. [PubMed: 30842662]
18. Wu J, Dobbs N, Yang K, and Yan N (2020). Interferon-Independent Activities of Mammalian STING Mediate Antiviral Response and Tumor Immune Evasion. Immunity 53, 115–126 e115. 10.1016/j.immuni.2020.06.009. [PubMed: 32640258]
19. Zhang R, Kang R, and Tang D (2022). STING1 in Different Organelles: Location Dictates Function. Front Immunol 13, 842489. 10.3389/fimmu.2022.842489. [PubMed: 35371032]
20. Rothhammer V, and Quintana FJ (2019). The aryl hydrocarbon receptor: an environmental sensor integrating immune responses in health and disease. Nat Rev Immunol 19, 184–197. 10.1038/s41577-019-0125-8. [PubMed: 30718831]
21. Agus A, Planchais J, and Sokol H (2018). Gut Microbiota Regulation of Tryptophan Metabolism in Health and Disease. Cell Host Microbe 23, 716–724. 10.1016/j.chom.2018.05.003. [PubMed: 29902437]
22. Sun M, Ma N, He T, Johnston LJ, and Ma X (2020). Tryptophan (Trp) modulates gut homeostasis via aryl hydrocarbon receptor (AhR). Crit Rev Food Sci Nutr 60, 1760–1768. 10.1080/10408398.2019.1598334. [PubMed: 30924357]
23. Pernomian L, Duarte-Silva M, and de Barros Cardoso CR (2020). The Aryl Hydrocarbon Receptor (AHR) as a Potential Target for the Control of Intestinal Inflammation: Insights from an Immune and Bacteria Sensor Receptor. Clin Rev Allergy Immunol 59, 382–390. 10.1007/s12016-020-08789-3. [PubMed: 32279195]
24. Wang Y, Wang M, Djekidel MN, Chen H, Liu D, Alt FW, and Zhang Y (2021). eccDNAs are apoptotic products with high innate immunostimulatory activity. Nature 599, 308–314. 10.1038/s41586-021-04009-w. [PubMed: 34671165]
25. Erttmann SF, Swacha P, Aung KM, Brindefalk B, Jiang H, Hartlova A, Uhlin BE, Wai SN, and Gekara NO (2022). The gut microbiota prime systemic antiviral immunity via the cGAS-STING-IFN-I axis. Immunity 55, 847–861 e810. 10.1016/j.immuni.2022.04.006. [PubMed: 35545033]
26. Sauer JD, Sotelo-Troha K, von Moltke J, Monroe KM, Rae CS, Brubaker SW, Hyodo M, Hayakawa Y, Woodward JJ, Portnoy DA, and Vance RE (2011). The N-ethyl-N-nitrosourea-induced Goldenticket mouse mutant reveals an essential function of Sting in the in vivo interferon response to Listeria monocytogenes and cyclic dinucleotides. Infect Immun 79, 688–694. 10.1128/IAI.00999-10. [PubMed: 21098106]
27. Canesso MCC, Lemos L, Neves TC, Marim FM, Castro TBR, Veloso ES, Queiroz CP, Ahn J, Santiago HC, Martins FS, et al. (2018). The cytosolic sensor STING is required for intestinal homeostasis and control of inflammation. Mucosal Immunol 11, 820–834. 10.1038/mi.2017.88. [PubMed: 29346345]
28. Wu J, Chen YJ, Dobbs N, Sakai T, Liou J, Miner JJ, and Yan N (2019). STING-mediated disruption of calcium homeostasis chronically activates ER stress and primes T cell death. J Exp Med 216, 867–883. 10.1084/jem.20182192. [PubMed: 30886058]
29. Zhang H, Zeng L, Xie M, Liu J, Zhou B, Wu R, Cao L, Kroemer G, Wang H, Billiar TR, et al. (2020). TMEM173 Drives Lethal Coagulation in Sepsis. Cell Host Microbe 27, 556–570 e556. 10.1016/j.chom.2020.02.004. [PubMed: 32142632]

30. Lee JH, Wada T, Febbraio M, He J, Matsubara T, Lee MJ, Gonzalez FJ, and Xie W (2010). A novel role for the dioxin receptor in fatty acid metabolism and hepatic steatosis. Gastroenterology 139, 653–663. 10.1053/j.gastro.2010.03.033. [PubMed: 20303349]

31. Esser C, and Rannug A (2015). The aryl hydrocarbon receptor in barrier organ physiology, immunology, and toxicology. Pharmacol Rev 67, 259–279. 10.1124/pr.114.009001. [PubMed: 25657351]

32. Tanaka Y, and Chen ZJ (2012). STING specifies IRF3 phosphorylation by TBK1 in the cytosolic DNA signaling pathway. Sci Signal 5, ra20. 10.1126/scisignal.2002521. [PubMed: 22394562]

33. Walczak K, Langner E, Makuch-Kocka A, Szelest M, Szalast K, Marciniak S, and Plech T (2020). Effect of Tryptophan-Derived AhR Ligands, Kynurenine, Kynurenic Acid and FICZ, on Proliferation, Cell Cycle Regulation and Cell Death of Melanoma Cells-In Vitro Studies. Int J Mol Sci 21. 10.3390/ijms21217946.

34. Fallarino F, Grohmann U, Vacca C, Bianchi R, Orabona C, Spreca A, Fioretti MC, and Puccetti P (2002). T cell apoptosis by tryptophan catabolism. Cell Death Differ 9, 1069–1077. 10.1038/sj.cdd.4401073. [PubMed: 12232795]

35. Dixon CR, Malik P, de Las Heras JI, Saiz-Ros N, de Lima Alves F, Tingey M, Gaunt E, Richardson AC, Kelly DA, Goldberg MW, et al. (2021). STING nuclear partners contribute to innate immune signaling responses. iScience 24, 103055. 10.1016/j.isci.2021.103055. [PubMed: 34541469]

36. Liu Y, Jesus AA, Marrero B, Yang D, Ramsey SE, Sanchez GAM, Tenbrock K, Wittkowski H, Jones OY, Kuehn HS, et al. (2014). Activated STING in a vascular and pulmonary syndrome. N Engl J Med 371, 507–518. 10.1056/NEJMoa1312625. [PubMed: 25029335]

37. Haag SM, Gulen MF, Reymond L, Gibelin A, Abrami L, Decout A, Heymann M, van der Goot FG, Turcatti G, Behrendt R, and Ablasser A (2018). Targeting STING with covalent small-molecule inhibitors. Nature 559, 269–273. 10.1038/s41586-018-0287-8. [PubMed: 29973723]

38. Lin B, Berard R, Al Rasheed A, Aladba B, Kranzusch PJ, Henderlight M, Grom A, Kahle D, Torreggiani S, Aue AG, et al. (2020). A novel STING1 variant causes a recessive form of STING-associated vasculopathy with onset in infancy (SAVI). J Allergy Clin Immunol 146, 1204–1208 e1206. 10.1016/j.jaci.2020.06.032. [PubMed: 32673614]

39. Melki I, Rose Y, Uggenti C, Van Eyck L, Fremond ML, Kitabayashi N, Rice GI, Jenkinson EM, Boulai A, Jeremiah N, et al. (2017). Disease-associated mutations identify a novel region in human STING necessary for the control of type I interferon signaling. J Allergy Clin Immunol 140, 543–552 e545. 10.1016/j.jaci.2016.10.031. [PubMed: 28087229]

40. Jafari R, Almqvist H, Axelsson H, Ignatushchenko M, Lundback T, Nordlund P, and Martinez Molina D (2014). The cellular thermal shift assay for evaluating drug target interactions in cells. Nat Protoc 9, 2100–2122. 10.1038/nprot.2014.138. [PubMed: 25101824]

41. Zhang H, Deng T, Liu R, Ning T, Yang H, Liu D, Zhang Q, Lin D, Ge S, Bai M, et al. (2020). CAF secreted miR-522 suppresses ferroptosis and promotes acquired chemo-resistance in gastric cancer. Mol Cancer 19, 43. 10.1186/s12943-020-01168-8. [PubMed: 32106859]

42. Zhao B, Du F, Xu P, Shu C, Sankaran B, Bell SL, Liu M, Lei Y, Gao X, Fu X, et al. (2019). A conserved PLPLRT/SD motif of STING mediates the recruitment and activation of TBK1. Nature 569, 718–722. 10.1038/s41586-019-1228-x. [PubMed: 31118511]

43. Kewley RJ, Whitelaw ML, and Chapman-Smith A (2004). The mammalian basic helix-loop-helix/PAS family of transcriptional regulators. Int J Biochem Cell Biol 36, 189–204. 10.1016/s1357-2725(03)00211-5. [PubMed: 14643885]

44. Taylor BL, and Zhulin IB (1999). PAS domains: internal sensors of oxygen, redox potential, and light. Microbiol Mol Biol Rev 63, 479–506. 10.1128/MMBR.63.2.479-506.1999. [PubMed: 10357859]

45. Beischlag TV, Luis Morales J, Hollingshead BD, and Perdew GH (2008). The aryl hydrocarbon receptor complex and the control of gene expression. Crit Rev Eukaryot Gene Expr 18, 207–250. 10.1615/critreveukargeneexpr.v18.i3.20. [PubMed: 18540824]

46. Taylor RT, Wang F, Hsu EL, and Hankinson O (2009). Roles of coactivator proteins in dioxin induction of CYP1A1 and CYP1B1 in human breast cancer cells. Toxicol Sci 107, 1–8. 10.1093/toxsci/kfn217. [PubMed: 18842620]

47. Seok SH, Lee W, Jiang L, Molugu K, Zheng A, Li Y, Park S, Bradfield CA, and Xing Y (2017). Structural hierarchy controlling dimerization and target DNA recognition in the AHR transcriptional complex. Proc Natl Acad Sci U S A 114, 5431–5436. 10.1073/pnas.1617035114. [PubMed: 28396409]
48. Lindebro MC, Poellinger L, and Whitelaw ML (1995). Protein-protein interaction via PAS domains: role of the PAS domain in positive and negative regulation of the bHLH/PAS dioxin receptor-Arnt transcription factor complex. EMBO J 14, 3528–3539. 10.1002/j.1460-2075.1995.tb07359.x. [PubMed: 7628454]
49. Brunnberg S, Pettersson K, Rydin E, Matthews J, Hanberg A, and Pongratz I (2003). The basic helix-loop-helix-PAS protein ARNT functions as a potent coactivator of estrogen receptor-dependent transcription. Proc Natl Acad Sci U S A 100, 6517–6522. 10.1073/pnas.1136688100. [PubMed: 12754377]
50. Cheradame L, Guerrera IC, Gaston J, Schmitt A, Jung V, Goudin N, Pouillard M, Radosevic-Robin N, Modesti M, Judde JG, et al. (2021). STING protects breast cancer cells from intrinsic and genotoxic-induced DNA instability via a non-canonical, cell-autonomous pathway. Oncogene 40, 6627–6640. 10.1038/s41388-021-02037-4. [PubMed: 34625708]
51. Yang J, Zhang L, Erbel PJ, Gardner KH, Ding K, Garcia JA, and Bruick RK (2005). Functions of the Per/ARNT/Sim domains of the hypoxia-inducible factor. J Biol Chem 280, 36047–36054. 10.1074/jbc.M501755200. [PubMed: 16129688]
52. Erbel PJ, Card PB, Karakuzu O, Bruick RK, and Gardner KH (2003). Structural basis for PAS domain heterodimerization in the basic helix--loop--helix-PAS transcription factor hypoxia-inducible factor. Proc Natl Acad Sci U S A 100, 15504–15509. 10.1073/pnas.2533374100. [PubMed: 14668441]
53. Marinelli L, Martin-Gallausiaux C, Bourhis JM, Beguet-Crespel F, Blottiere HM, and Lapaque N (2019). Identification of the novel role of butyrate as AhR ligand in human intestinal epithelial cells. Sci Rep 9, 643. 10.1038/s41598-018-37019-2. [PubMed: 30679727]
54. Abron JD, Singh NP, Mishra MK, Price RL, Nagarkatti M, Nagarkatti PS, and Singh UP (2018). An endogenous aryl hydrocarbon receptor ligand, ITE, induces regulatory T cells and ameliorates experimental colitis. Am J Physiol Gastrointest Liver Physiol 315, G220–G230. 10.1152/ajpgi.00413.2017. [PubMed: 29672155]
55. Monteleone I, Rizzo A, Sarra M, Sica G, Sileri P, Biancone L, MacDonald TT, Pallone F, and Monteleone G (2011). Aryl hydrocarbon receptor-induced signals up-regulate IL-22 production and inhibit inflammation in the gastrointestinal tract. Gastroenterology 141, 237–248, 248 e231. 10.1053/j.gastro.2011.04.007. [PubMed: 21600206]
56. Villanacci V, Antonelli E, Geboes K, Casella G, and Bassotti G (2013). Histological healing in inflammatory bowel disease: a still unfulfilled promise. World J Gastroenterol 19, 968–978. 10.3748/wjg.v19.i7.968. [PubMed: 23467585]
57. Zuo T, and Ng SC (2018). The Gut Microbiota in the Pathogenesis and Therapeutics of Inflammatory Bowel Disease. Front Microbiol 9, 2247. 10.3389/fmicb.2018.02247. [PubMed: 30319571]
58. Michaudel C, Danne C, Agus A, Magniez A, Aucouturier A, Spatz M, Lefevre A, Kirchgesner J, Rolhion N, Wang Y, et al. (2022). Rewiring the altered tryptophan metabolism as a novel therapeutic strategy in inflammatory bowel diseases. Gut. 10.1136/gutjnl-2022-327337.
59. Gao Z, Chen KY, Mueller O, Zhang H, Rakhilin N, Chen J, and Shen X (2018). Microbiota of Inflammatory Bowel Disease Models. Annu Int Conf IEEE Eng Med Biol Soc 2018, 2374–2377. 10.1109/EMBC.2018.8512848. [PubMed: 30440884]
60. Cai J, Sun L, and Gonzalez FJ (2022). Gut microbiota-derived bile acids in intestinal immunity, inflammation, and tumorigenesis. Cell Host Microbe 30, 289–300. 10.1016/j.chom.2022.02.004. [PubMed: 35271802]
61. Lavelle A, and Sokol H (2020). Gut microbiota-derived metabolites as key actors in inflammatory bowel disease. Nat Rev Gastroenterol Hepatol 17, 223–237. 10.1038/s41575-019-0258-z. [PubMed: 32076145]
62. Belkaid Y, and Hand TW (2014). Role of the microbiota in immunity and inflammation. Cell 157, 121–141. 10.1016/j.cell.2014.03.011. [PubMed: 24679531]

63. Wang W, Hu D, Wu C, Feng Y, Li A, Liu W, Wang Y, Chen K, Tian M, Xiao F, et al. (2020). STING promotes NLRP3 localization in ER and facilitates NLRP3 deubiquitination to activate the inflammasome upon HSV-1 infection. PLoS Pathog 16, e1008335. 10.1371/journal.ppat.1008335. [PubMed: 32187211]

64. Gonugunta VK, Sakai T, Pokatayev V, Yang K, Wu J, Dobbs N, and Yan N (2017). Trafficking-Mediated STING Degradation Requires Sorting to Acidified Endolysosomes and Can Be Targeted to Enhance Anti-tumor Response. Cell Rep 21, 3234–3242. 10.1016/j.celrep.2017.11.061. [PubMed: 29241549]

65. Gaidt MM, Ebert TS, Chauhan D, Ramshorn K, Pinci F, Zuber S, O'Duill F, Schmid-Burgk JL, Hoss F, Buhmann R, et al. (2017). The DNA Inflammasome in Human Myeloid Cells Is Initiated by a STING-Cell Death Program Upstream of NLRP3. Cell 171, 1110–1124 e1118. 10.1016/j.cell.2017.09.039. [PubMed: 29033128]

66. Nazmi A, Mukhopadhyay R, Dutta K, and Basu A (2012). STING mediates neuronal innate immune response following Japanese encephalitis virus infection. Sci Rep 2, 347. 10.1038/srep00347. [PubMed: 22470840]

67. Zhu L, Yang F, Wang L, Dong L, Huang Z, Wang G, Chen G, and Li Q (2021). Identification the ferroptosis-related gene signature in patients with esophageal adenocarcinoma. Cancer Cell Int 21, 124. 10.1186/s12935-021-01821-2. [PubMed: 33602233]

68. Malik P, Zuleger N, de las Heras JI, Saiz-Ros N, Makarov AA, Lazou V, Meinke P, Waterfall M, Kelly DA, and Schirmer EC (2014). NET23/STING promotes chromatin compaction from the nuclear envelope. PLoS One 9, e111851. 10.1371/journal.pone.0111851. [PubMed: 25386906]

69. Jeltema D, Abbott K, and Yan N (2023). STING trafficking as a new dimension of immune signaling. J Exp Med 220. 10.1084/jem.20220990.

70. Kuchitsu Y, Mukai K, Uematsu R, Takaada Y, Shinojima A, Shindo R, Shoji T, Hamano S, Ogawa E, Sato R, et al. (2023). STING signalling is terminated through ESCRT-dependent microautophagy of vesicles originating from recycling endosomes. Nat Cell Biol 25, 453–466. 10.1038/s41556-023-01098-9. [PubMed: 36918692]

71. Yu X, Zhang L, Shen J, Zhai Y, Jiang Q, Yi M, Deng X, Ruan Z, Fang R, Chen Z, et al. (2021). The STING phase-separator suppresses innate immune signalling. Nat Cell Biol 23, 330–340. 10.1038/s41556-021-00659-0. [PubMed: 33833429]

72. Hong Y, Jeong H, Park K, Lee S, Shim JY, Kim H, Song Y, Park S, Park HY, Kim VN, and Ahn K (2021). STING facilitates nuclear import of herpesvirus genome during infection. Proc Natl Acad Sci U S A 118. 10.1073/pnas.2108631118.

73. Kang J, Wu J, Liu Q, Wu X, Zhao Y, and Ren J (2022). Post-Translational Modifications of STING: A Potential Therapeutic Target. Front Immunol 13, 888147. 10.3389/fimmu.2022.888147. [PubMed: 35603197]

74. Bai J, and Liu F (2022). Nuclear cGAS: sequestration and beyond. Protein Cell 13, 90–101. 10.1007/s13238-021-00869-0. [PubMed: 34374004]

75. Shang G, Zhang C, Chen ZJ, Bai XC, and Zhang X (2019). Cryo-EM structures of STING reveal its mechanism of activation by cyclic GMP-AMP. Nature 567, 389–393. 10.1038/s41586-019-0998-5. [PubMed: 30842659]

76. de Jesus AJ, and Allen TW (2013). The role of tryptophan side chains in membrane protein anchoring and hydrophobic mismatch. Biochim Biophys Acta 1828, 864–876. 10.1016/j.bbamem.2012.09.009. [PubMed: 22989724]

77. McPhee MJ, Salsman J, Foster J, Thompson J, Mathavarajah S, Dellaire G, and Ridgway ND (2022). Running 'LAPS' Around nLD: Nuclear Lipid Droplet Form and Function. Front Cell Dev Biol 10, 837406. 10.3389/fcell.2022.837406. [PubMed: 35178392]

78. Malik P, Korfali N, Srsen V, Lazou V, Batrakou DG, Zuleger N, Kavanagh DM, Wilkie GS, Goldberg MW, and Schirmer EC (2010). Cell-specific and lamin-dependent targeting of novel transmembrane proteins in the nuclear envelope. Cell Mol Life Sci 67, 1353–1369. 10.1007/s00018-010-0257-2. [PubMed: 20091084]

79. Rogler G, Singh A, Kavanaugh A, and Rubin DT (2021). Extraintestinal Manifestations of Inflammatory Bowel Disease: Current Concepts, Treatment, and Implications for Disease

Management. Gastroenterology 161, 1118–1132. 10.1053/j.gastro.2021.07.042. [PubMed: 34358489]

80. Roda G, Chien Ng S, Kotze PG, Argollo M, Panaccione R, Spinelli A, Kaser A, Peyrin-Biroulet L, and Danese S (2020). Crohn's disease. Nat Rev Dis Primers 6, 22. 10.1038/s41572-020-0156-2. [PubMed: 32242028]
81. Kobayashi T, Siegmund B, Le Berre C, Wei SC, Ferrante M, Shen B, Bernstein CN, Danese S, Peyrin-Biroulet L, and Hibi T (2020). Ulcerative colitis. Nat Rev Dis Primers 6, 74. 10.1038/s41572-020-0205-x. [PubMed: 32913180]
82. Ahn J, Son S, Oliveira SC, and Barber GN (2017). STING-Dependent Signaling Underlies IL-10 Controlled Inflammatory Colitis. Cell Rep 21, 3873–3884. 10.1016/j.celrep.2017.11.101. [PubMed: 29281834]
83. Ma C, Yang D, Wang B, Wu C, Wu Y, Li S, Liu X, Lassen K, Dai L, and Yang S (2020). Gasdermin D in macrophages restrains colitis by controlling cGAS-mediated inflammation. Sci Adv 6, eaaz6717. 10.1126/sciadv.aaz6717. [PubMed: 32671214]
84. Martin GR, Blomquist CM, Henare KL, and Jirik FR (2019). Stimulator of interferon genes (STING) activation exacerbates experimental colitis in mice. Sci Rep 9, 14281. 10.1038/s41598-019-50656-5. [PubMed: 31582793]
85. Zhu Q, Man SM, Gurung P, Liu Z, Vogel P, Lamkanfi M, and Kanneganti TD (2014). Cutting edge: STING mediates protection against colorectal tumorigenesis by governing the magnitude of intestinal inflammation. J Immunol 193, 4779–4782. 10.4049/jimmunol.1402051. [PubMed: 25320273]
86. Damasceno LEA, Cebinelli GCM, Fernandes MF, Nascimento DC, Publio GA, Vinolo MAR, Oliveira SC, Sparwasser T, Cunha TM, Cunha FQ, and Alves-Filho JC (2022). STING is an intrinsic checkpoint inhibitor that restrains the T(H)17 cell pathogenic program. Cell Rep 39, 110838. 10.1016/j.celrep.2022.110838. [PubMed: 35613599]
87. Singh NP, Singh UP, Singh B, Price RL, Nagarkatti M, and Nagarkatti PS (2011). Activation of aryl hydrocarbon receptor (AhR) leads to reciprocal epigenetic regulation of FoxP3 and IL-17 expression and amelioration of experimental colitis. PLoS One 6, e23522. 10.1371/journal.pone.0023522. [PubMed: 21858153]
88. Oh-Oka K, Kojima Y, Uchida K, Yoda K, Ishimaru K, Nakajima S, Hemmi J, Kano H, Fujii-Kuriyama Y, Katoh R, et al. (2017). Induction of Colonic Regulatory T Cells by Mesalamine by Activating the Aryl Hydrocarbon Receptor. Cell Mol Gastroenterol Hepatol 4, 135–151. 10.1016/j.jcmgh.2017.03.010. [PubMed: 28593185]
89. Stockinger B, Shah K, and Wincent E (2021). AHR in the intestinal microenvironment: safeguarding barrier function. Nat Rev Gastroenterol Hepatol 18, 559–570. 10.1038/s41575-021-00430-8. [PubMed: 33742166]
90. Lee M, and Chang EB (2021). Inflammatory Bowel Diseases (IBD) and the Microbiome-Searching the Crime Scene for Clues. Gastroenterology 160, 524–537. 10.1053/j.gastro.2020.09.056. [PubMed: 33253681]
91. Takamura T, Harama D, Fukumoto S, Nakamura Y, Shimokawa N, Ishimaru K, Ikegami S, Makino S, Kitamura M, and Nakao A (2011). Lactobacillus bulgaricus OLL1181 activates the aryl hydrocarbon receptor pathway and inhibits colitis. Immunol Cell Biol 89, 817–822. 10.1038/icb.2010.165. [PubMed: 21321579]
92. Lamas B, Richard ML, Leducq V, Pham HP, Michel ML, Da Costa G, Bridonneau C, Jegou S, Hoffmann TW, Natividad JM, et al. (2016). CARD9 impacts colitis by altering gut microbiota metabolism of tryptophan into aryl hydrocarbon receptor ligands. Nat Med 22, 598–605. 10.1038/nm.4102. [PubMed: 27158904]
93. Zhu R, Gao C, Wang L, Zhang G, Zhang W, Zhang Z, Shen L, and Wang S (2018). Involvement of Aryl Hydrocarbon Receptor and Aryl Hydrocarbon Receptor Repressor in Helicobacter Pylori-related Gastric Pathogenesis. J Cancer 9, 2757–2764. 10.7150/jca.26083. [PubMed: 30087718]
94. Pirzadeh M, Khalili N, and Rezaei N (2022). The interplay between aryl hydrocarbon receptor, H. pylori, tryptophan, and arginine in the pathogenesis of gastric cancer. Int Rev Immunol 41, 299–312. 10.1080/08830185.2020.1851371. [PubMed: 33236682]

95. Fling RR, and Zacharewski TR (2021). Aryl Hydrocarbon Receptor (AhR) Activation by 2,3,7,8-Tetrachlorodibenzo-p-Dioxin (TCDD) Dose-Dependently Shifts the Gut Microbiome Consistent with the Progression of Non-Alcoholic Fatty Liver Disease. Int J Mol Sci 22. 10.3390/ijms222212431.

96. Kumar P, and Kolls JK (2016). Lymphocyte Isolation, Th17 Cell Differentiation, Activation, and Staining. Bio Protoc 6. 10.21769/BioProtoc.2047.

97. Liu Y, Yang X, Gan J, Chen S, Xiao ZX, and Cao Y (2022). CB-Dock2: improved protein-ligand blind docking by integrating cavity detection, docking and homologous template fitting. Nucleic Acids Res 50, W159–W164. 10.1093/nar/gkac394. [PubMed: 35609983]

98. de Vries SJ, van Dijk M, and Bonvin AM (2010). The HADDOCK web server for data-driven biomolecular docking. Nat Protoc 5, 883–897. 10.1038/nprot.2010.32. [PubMed: 20431534]

99. Klindworth A, Pruesse E, Schweer T, Peplies J, Quast C, Horn M, and Glockner FO (2013). Evaluation of general 16S ribosomal RNA gene PCR primers for classical and next-generation sequencing-based diversity studies. Nucleic Acids Res 41, e1. 10.1093/nar/gks808. [PubMed: 22933715]

100. Shen W, and Ren H (2021). TaxonKit: A practical and efficient NCBI taxonomy toolkit. J Genet Genomics 48, 844–850. 10.1016/j.jgg.2021.03.006. [PubMed: 34001434]

101. Raudvere U, Kolberg L, Kuzmin I, Arak T, Adler P, Peterson H, and Vilo J (2019). g:Profiler: a web server for functional enrichment analysis and conversions of gene lists (2019 update). Nucleic Acids Res 47, W191–W198. 10.1093/nar/gkz369. [PubMed: 31066453]

102. Ge SX, Son EW, and Yao R (2018). iDEP: an integrated web application for differential expression and pathway analysis of RNA-Seq data. BMC Bioinformatics 19, 534. 10.1186/s12859-018-2486-6. [PubMed: 30567491]

103. Subramanian A, Tamayo P, Mootha VK, Mukherjee S, Ebert BL, Gillette MA, Paulovich A, Pomeroy SL, Golub TR, Lander ES, and Mesirov JP (2005). Gene set enrichment analysis: a knowledge-based approach for interpreting genome-wide expression profiles. Proc Natl Acad Sci U S A 102, 15545–15550. 10.1073/pnas.0506580102. [PubMed: 16199517]

104. Chong J, Liu P, Zhou G, and Xia J (2020). Using MicrobiomeAnalyst for comprehensive statistical, functional, and meta-analysis of microbiome data. Nat Protoc 15, 799–821. 10.1038/s41596-019-0264-1. [PubMed: 31942082]

105. Douglas GM, Maffei VJ, Zaneveld JR, Yurgel SN, Brown JR, Taylor CM, Huttenhower C, and Langille MGI (2020). PICRUSt2 for prediction of metagenome functions. Nat Biotechnol 38, 685–688. 10.1038/s41587-020-0548-6. [PubMed: 32483366]

106. Chen T, Liu Y-X, and Huang L (2022). ImageGP: An easy-to-use data visualization web server for scientific researchers. iMeta 1, e5. 10.1002/imt2.5.

Highlights

- Nuclear STING1 activates AHR independently of the known ARNT pathway.
- Competitive interplay exists between the STING1-AHR and CGAS-STING1 pathways.
- The CBD of STING1 interacts with the N-terminal domain of AHR.
- STING1 is essential for AHR-mediated protection against IBD in mice.

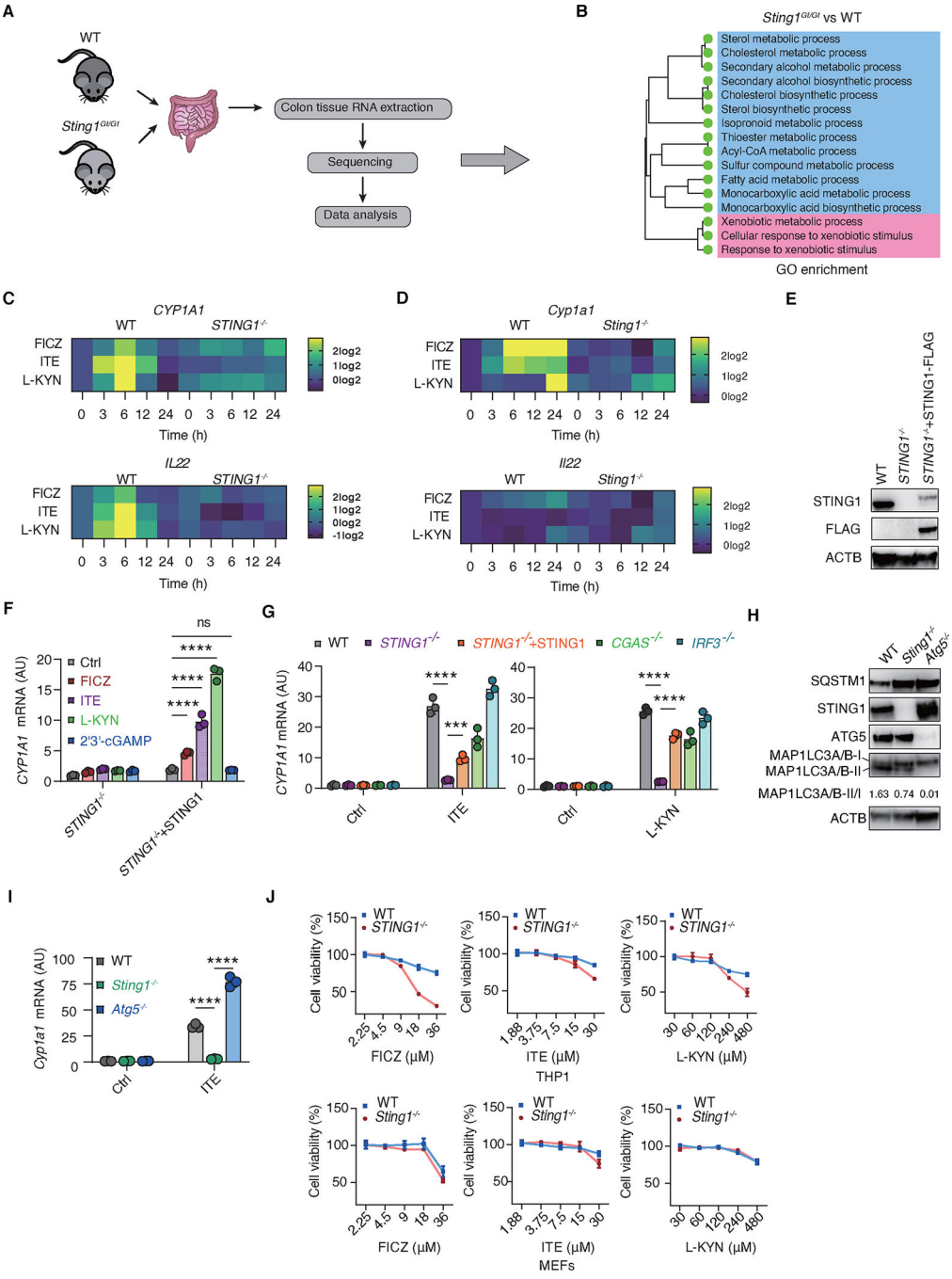

Figure 1. STING1 promotes AHR activation independent of its canonical functions, see also Figure S1 and Table S1.

(A) Schematic diagram of the workflow for next-generation sequencing analysis of colon tissue from wild-type (WT) and *Sting1*$^{Gt/Gt}$ mice.

(B) Gene Ontology (GO) biological process enrichment analysis of differentially expressed genes in mouse colon tissue. Shown are pathways downregulated in the *Sting1*$^{Gt/Gt}$ group versus WT mice group. Shown in orange are pathways related to xenobiotic metabolism. Shown in blue are pathways related to lipid metabolism and others.

(C) qPCR analysis of *CYP1A1* and *IL22* gene expression in WT and *STING1*$^{-/-}$ THP1 cells after treating with AHR ligands, including FICZ (18 μM), ITE (15 μM), and L-KYN (240 μM) for 3–24 h. Ligand dosage is based on the dosage used in most literature. Data are shown as heat maps of gene expression (log_2 normalized relative fold change) induced by AHR ligands compared to DMSO control. Each block represents the mean of 3 biologically independent samples.

(D) qPCR analysis of *Cyp1a1* and *Il22* gene expression in wild-type (WT) and *Sting1*$^{-/-}$ MEFs following treatment with AHR ligands (FICZ, ITE, and L-KYN) at specified dosages (18 μM, 15 μM, and 240 μM, respectively) for 3–24 h. Data are shown as heat maps of gene expression (log_2 normalized relative fold change) induced by AHR ligands compared to the DMSO control. Each block represents the mean of three independent biological samples.

(E) Western blot analysis of the indicated proteins in WT, *STING1*$^{-/-}$, and *STING1*$^{-/-}$ THP1 cells transfected with *STING1*-FLAG expression plasmid.

(F) qPCR analysis of *CYP1A1* gene expression in the indicated THP1 cells after treatment with AHR ligands (FICZ, ITE, and L-KYN) and 2'3'-cGAMP (10 μg/ml) for 6 h (n=3 biologically independent samples; ****P < 0.0001; two-way ANOVA with Tukey's multiple comparisons test; data are presented as mean ± SD).

(G) qPCR analysis of *CYP1A1* gene expression in the indicated THP1 cells after treatment with AHR ligands for 6 h (n=3 biologically independent samples; ***P < 0.0005, ****P <0.0001; two-way ANOVA with Tukey's multiple comparisons test; data are presented as mean ± SD).

(H) Western blot analysis of protein expression in the indicated MEFs.

(I) qPCR analysis of *Cyp1a1* gene expression in the indicated MEFs following treatment with ITE (15 μM) for 24 h (n=3 biologically independent samples; ****P < 0.0001; two-way ANOVA with Tukey's multiple comparisons test; data are presented as mean ± SD).

(J) Analysis of cell viability in THP1 cells following treatment with AHR ligands (FICZ, ITE, and L-KYN) for 6 h or in MEFs following treatment with AHR ligands (FICZ, ITE, and L-KYN) at the indicated dose for 24 h (n=3 biologically independent samples; data are presented as mean ± SD).

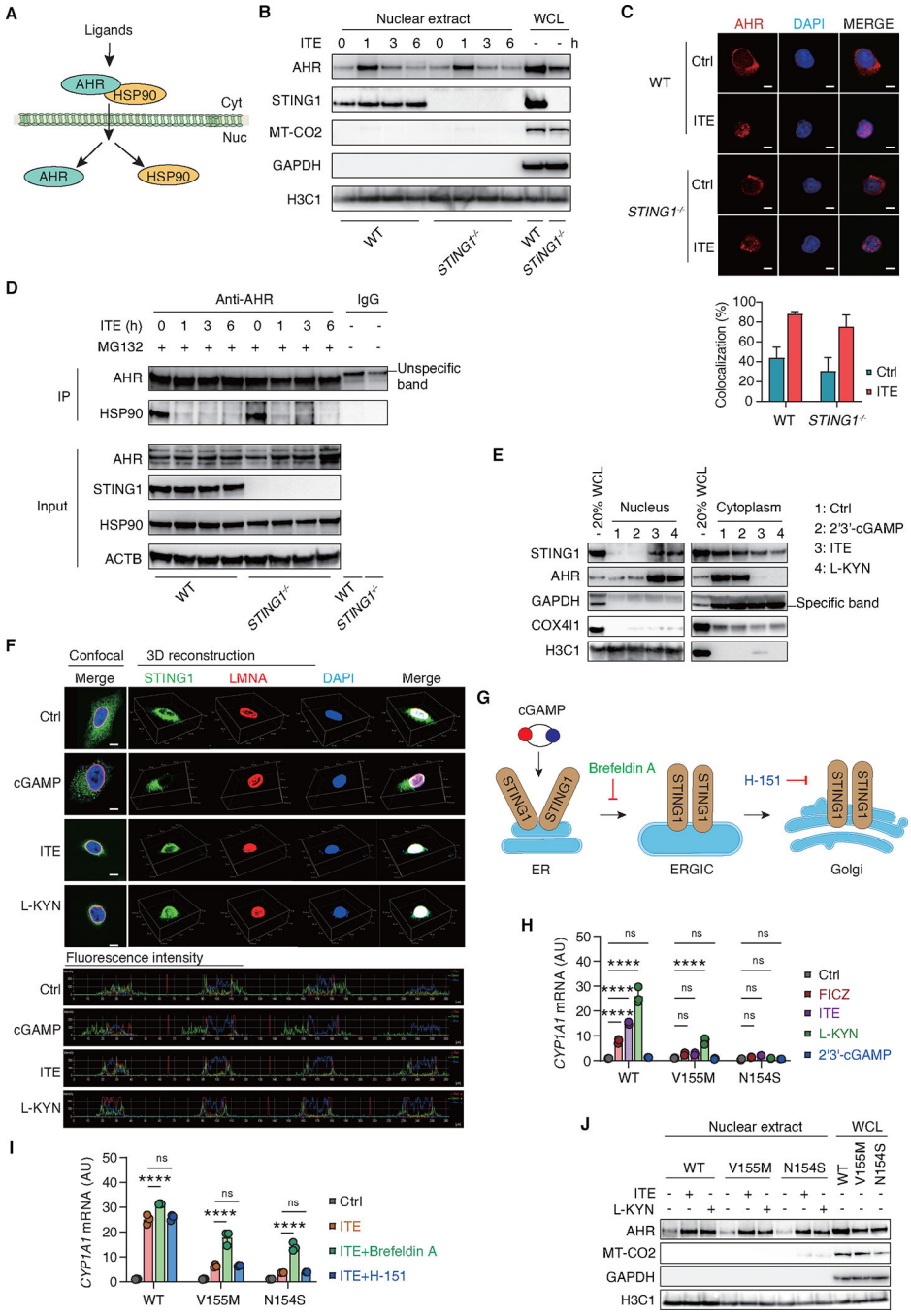

Figure 2. STING1 mediates AHR activation in the nucleus, see also Figure S2.

(A) Schematic diagram of the mechanism by which AHR translocates to the nucleus and dissociates from HSP90. AHR, aryl hydrocarbon receptor; HSP90, heat shock protein 90. **(B)** Western blot analysis of the indicated proteins (GAPDH [cytosolic marker], MT-CO2 [mitochondrial marker], and H3C1 [nuclear marker]) in whole cell lysates (WCL) or nuclear extract of WT and *STING1*$^{-/-}$ THP1 cells following treatment with ITE (15 μM) for 1–6 h.

(C) Immunofluorescence analysis of the colocalization between AHR (red) and the nucleus in the indicated THP1 cells following treatment with ITE (15 μM) for 1 h. Nuclei are stained with DAPI (blue). Scale bar: 5 μm. The data are presented from 5 fields.

(D) Immunoprecipitation (IP) analysis of AHR-binding proteins in the indicated THP1 cells following treatment with ITE (15 μM) in the presence of the proteasome inhibitor MG132 (20 μM) for 1–6 h. IB, immunoblot.

(E) Western blot analysis of protein expression in WCL or cell fractionation (cytoplasm and nucleus) of THP1 cells following treatment with 2'3'-cGAMP (10 μg/mL), ITE (15 μM), and L-KYN (240 μM) for 1 h.

(F) Immunofluorescence analysis was performed to examine the colocalization of the nuclear envelope marker LMNA with STING1 (green) in HeLa cells stably expressing the STING1-GFP fusion protein. The cells were treated with cGAMP (10 μg/mL), ITE (15 μM), or L-KYN (240 μM) for 1 h. Nuclei were stained with DAPI (blue). Confocal microscopy was used to capture series z-stack images, followed by 3D reconstruction and fluorescence intensity analysis. Representative optical sections from the z-stack are shown. Scale bar: 5 μm.

(G) Schematic illustration of the mechanism by which brefeldin A and H-151 inhibit translocation of STING1 in the ER, ERGIC, and Golgi.

(H) qPCR analysis of *CYP1A1* gene expression in WT and STING1-mutant (V155M and N154S) THP1 cells following treatment with 2'3'-cGAMP (10 μg/mL), FICZ (18 μM), ITE (15 μM), and L-KYN (240 μM) for 6 h (n=3 biologically independent samples; ****P < 0.0001; two-way ANOVA with Tukey's multiple comparisons test; data are presented as mean ± SD).

(I) qPCR analysis of *CYP1A1* gene expression in WT and STING1-mutant THP1 cells following treatment with ITE (15 μM) in the absence or presence of brefeldin A (2 μM) or H-151 (0.5 μM) for 6 h (n=3 biologically independent samples; ****P < 0.0001; two-way ANOVA with Tukey's multiple comparisons test; data are presented as mean ± SD).

(J) Western blot analysis of the indicated protein expression (GAPDH, MT-CO2, and H3C1) in WCL or nuclear extract of the indicated THP1 cells following treatment with ITE (15 μM) for 1 h.

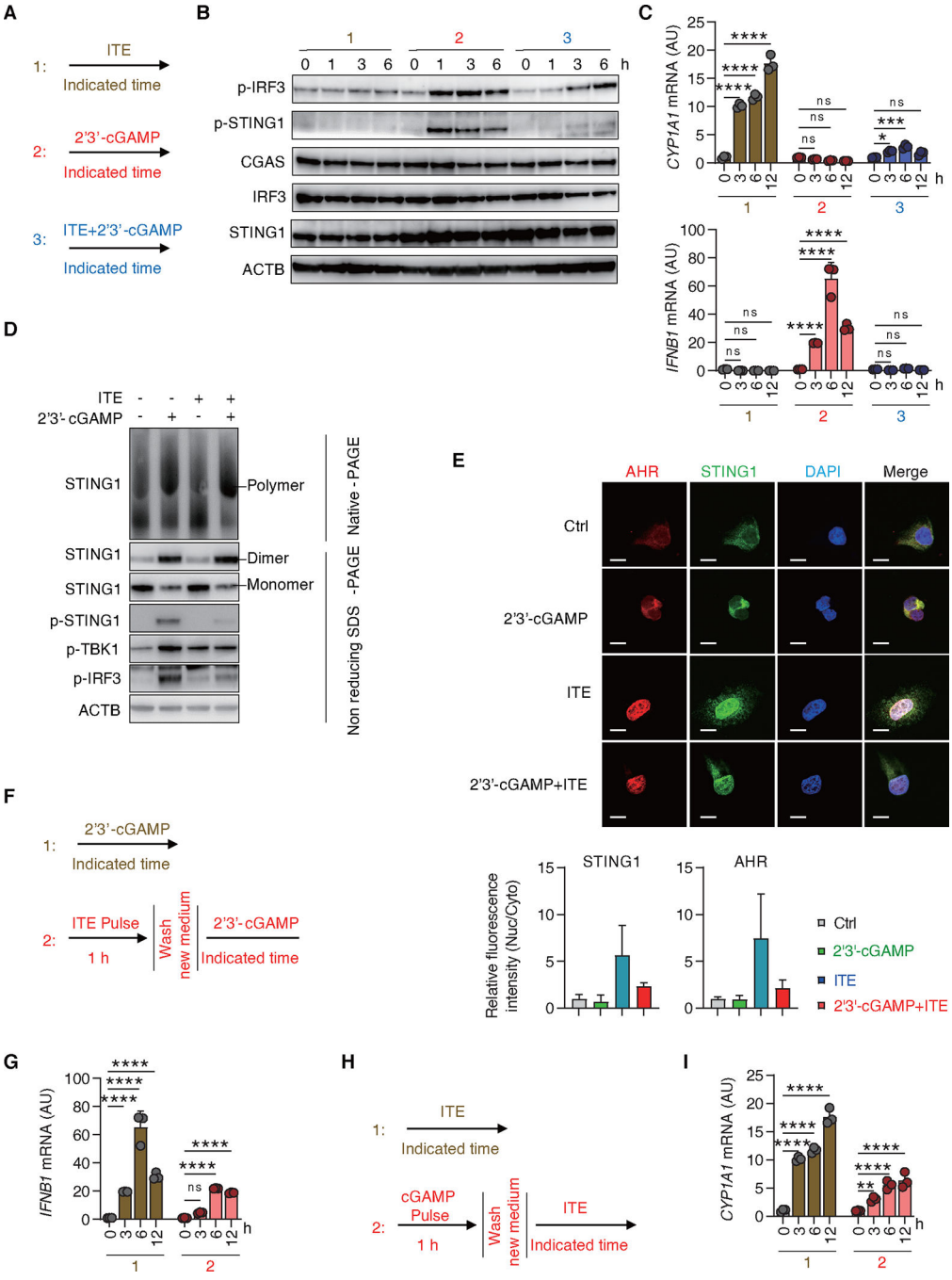

Figure 3. Competition between the STING1-AHR and CGAS-STING1 pathways, see also Figure S3.

(A) Schematic diagram of ITE and 2'3'-cGAMP treatment alone or together.

(B) Western blot analysis of the indicated proteins in THP1 cells following treatment with ITE (15 μM) (1, brown), 2'3'-cGAMP (10 μg/mL) (2, red), or ITE (15 μM) plus 2'3'-cGAMP (10 μg/mL) (3, blue) for 1–6 h.

(C) qPCR analysis of *CYP1A1* or *IFNB1* gene expression in THP1 cells following treatment with ITE (15 μM) (1, brown), 2'3'-cGAMP (10 μg/mL) (2, red), or ITE (15 μM) plus

2’3’-cGAMP (10 μg/mL) (3, blue) for 3–12 h (n=3 biologically independent samples; *P < 0.05, ***P < 0.0005, ****P < 0.0001; two-way ANOVA with Tukey’s multiple comparisons test; data are presented as mean ± SD).

(D) Western blot analysis of the indicated proteins in THP1 cells following treatment with ITE (15 μM) in the absence or presence of 2’3’-cGAMP (10 μg/mL) for 1 h by native-page or non-reducing SDS-PAGE.

(E) Immunofluorescence analysis of distribution of AHR (red) and STING1 (green) in HeLa cells stably expressing the STING1-GFP fusion protein following treatment with ITE (15 μM) and/or 2’3 ‘-cGAMP (10 μg/mL) for 1 h. Nuclei are stained with DAPI (blue). Scale bar: 20 μm. The semi-quantitative data are presented as the mean ± SD of 5 fields of view.

(F) Schematic diagram of 2’3’-cGAMP treatment or ITE pulse before 2’3’-cGAMP treatment.

(G) qPCR analysis of *IFNB1* gene expression in THP1 cells following treatment with 2’3’-cGAMP (10 μg/mL) (1, brown) or ITE (15 μM) pulse before 2’3’-cGAMP (10 μg/mL) treatment (2, red) (n=3 biologically independent samples; ****P < 0.0001; two-way ANOVA with Tukey’s multiple comparisons test; data are presented as mean ± SD).

(H) Schematic diagram of ITE treatment or 2’3’-cGAMP pulse before ITE treatment.

(I) qPCR analysis of *CYP1A1* gene expression in THP1 cells following treatment with ITE (15 μM) (1, brown) or 2’3’-cGAMP (10 μg/mL) pulse before ITE (15 μM) treatment (2, red) (n=3 biologically independent samples; **P < 0.005, ****P < 0.0001; two-way ANOVA with Tukey’s multiple comparisons test; data are presented as mean ± SD).

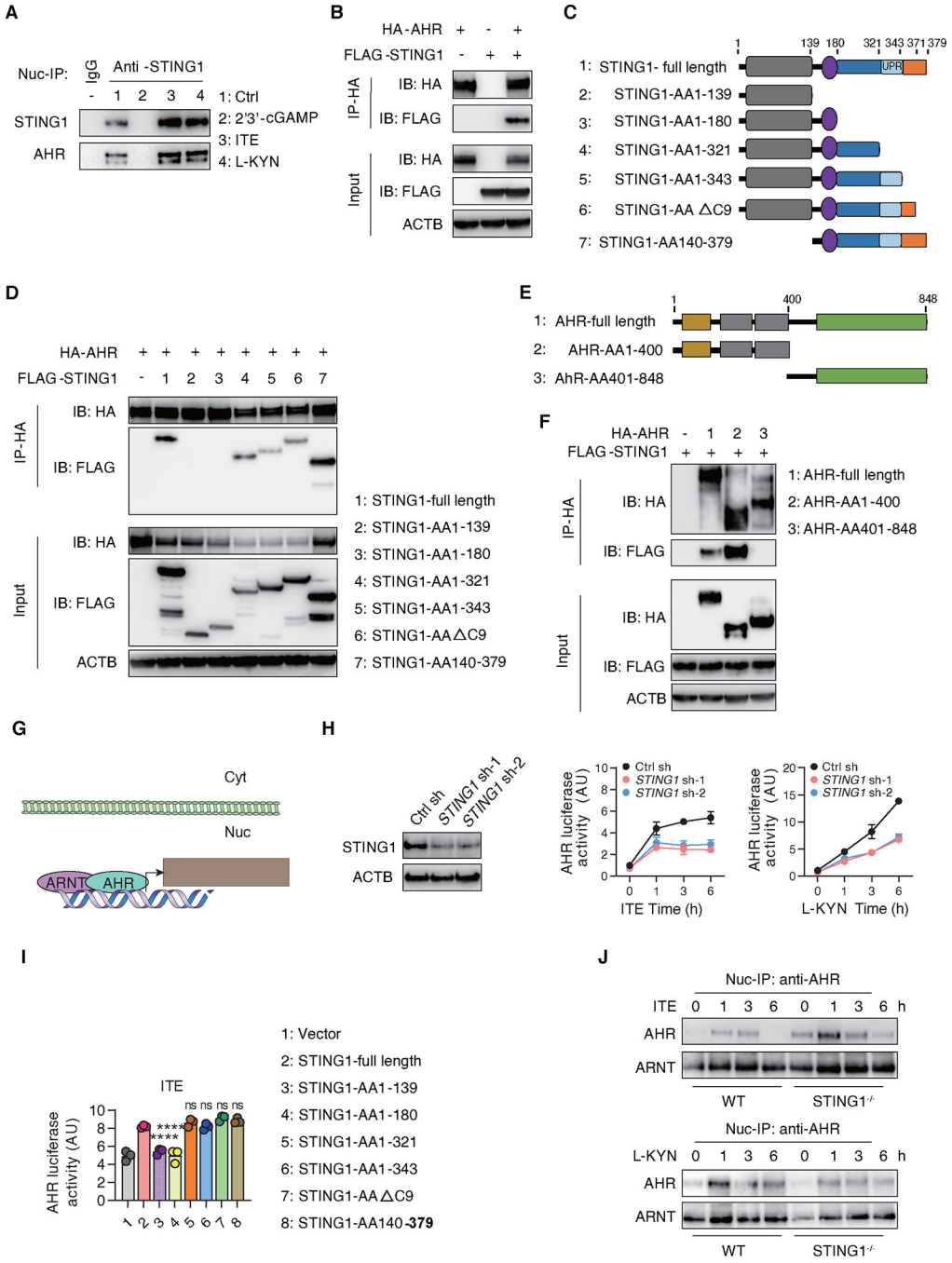

Figure 4. Structural basis of STING1-AHR complex formation, see also Figure S4.

(A) Nuclear immunoprecipitation (IP) analysis of the interaction between STING and AHR in THP1 cells following treatment with 2'3'-cGAMP (10 μg/mL), ITE (15 μM), and L-KYN (240 μM) for 1 h.

(B) HEK293T cells were co-transfected with the indicated FLAG-tagged STING1 and HA-tagged AHR expression plasmid. Cell lysates were subjected to immunoprecipitation (IP) with anti-HA antibodies to assay the interaction between AHR and STING1.

(C) Schematic showing domain structure of WT and human STING1 mutants. TM, transmembrane segment; DD, dimerization domain; CBD, CDNs binding domain; UPR, unfolded protein response domain; CTT, C-terminal tail.

(D) HEK293T cells were co-transfected with the indicated FLAG-tagged STING1 and HA-tagged AHR expression plasmids. Cell lysates were subjected to immunoprecipitation (IP) with anti-HA antibodies to detect the interaction between STING1 and AHR.

(E) Schematic showing domain structure of WT and human AHR mutants. bHLH, basic helix-loop-helix domain; PAS-A, Per-ARNT-Sim domain A; PAS-B, Per-ARNT-Sim domain B; TAD, transactivation domain.

(F) HEK293T cells were co-transfected with the indicated FLAG-tagged STING1 and HA-tagged AHR expression plasmids. Cell lysates were subjected to immunoprecipitation (IP) with anti-HA antibodies to detect the interaction between STING1 and AHR.

(G) Schematic of the mechanism by which the AHR and ARNT transcription complexes regulate gene expression in the nucleus. AHR, aryl hydrocarbon receptor; ARNT, aryl hydrocarbon receptor nuclear transporter.

(H) WT and *STING1*-deficient HT29-Lucia™ AHR (HT-29 lucia) cells were treated with ITE (15 μM) or L-KYN (240 μM) for 1–6 h and then transcriptional activity of AHR was assayed (n=3 biologically independent samples; data are presented as mean ± SD).

(I) Analysis of AHR transcriptional activity in the indicated HT-29 lucia cells transfected with FLAG-tagged STING1 or STING1 mutants following treatment with ITE (15 μM) for 6 h (n=3 biologically independent samples; ****$P < 0.0001$; two-way ANOVA with Tukey's multiple comparisons test; data are presented as mean ± SD).

(J) Nuclear immunoprecipitation (IP) analysis of the interaction between AHR and ARNT in indicated THP1 cells following treatment with ITE (15 μM) or L-KYN (240 μM) for 1–6 h.

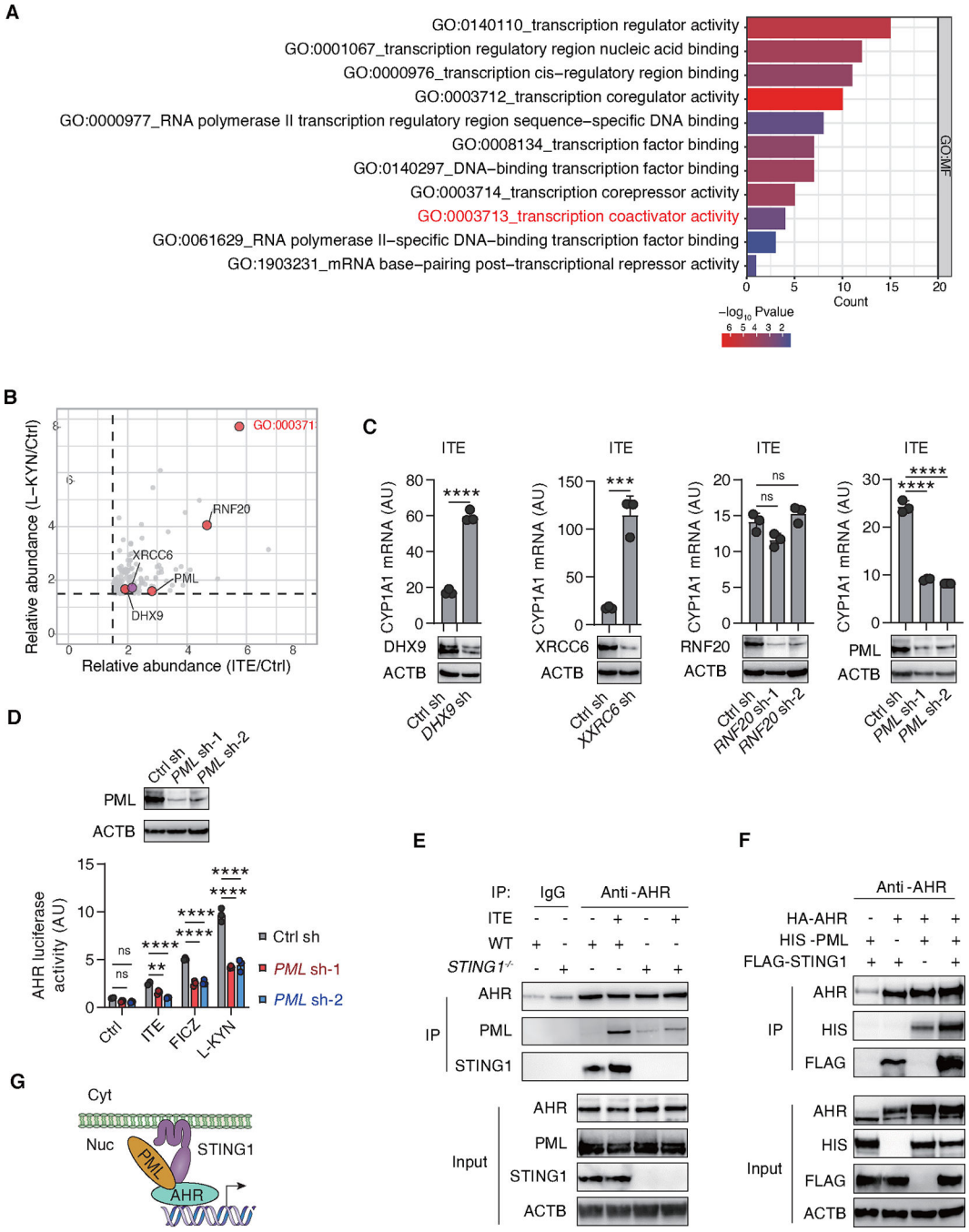

Figure 5. STING1-mediated AHR activation requires PML, see also Figure S5.

(A) Gene Ontology (GO) enrichment analysis of nuclear STING1-binding proteins in transcriptional pathways.

(B) Mass spectrometry analysis of the nuclear binding proteins of STING1 after treatment with ITE (15 μM) for 1 h.

(C) qPCR analysis of *CYP1A1* gene expression in the indicated THP1 cells after treatment with ITE (15 μM) for 6 h (n=3 biologically independent samples; **P < 0.005, ***P <

0.0005, ****P < 0.0001; two-way ANOVA with Tukey's multiple comparisons test; data are presented as mean ± SD).

(D) Analysis of transcriptional activity of AHR in the indicated HT-29 lucia cells treated with FICZ (18 μM), ITE (15 μM), and L-KYN (240 μM) for 6 h (n=3 biologically independent samples; **P < 0.005, ****P < 0.0001; two-way ANOVA with Tukey's multiple comparisons test; data are presented as mean ± SD).

(E) Immunoprecipitation (IP) analysis of AHR-binding proteins in WT and *STING1*$^{-/-}$ THP1 cells following treatment with ITE (15 μM) for 1 h.

(F) HEK293T cells were co-transfected with the indicated FLAG-tagged STING1, HA-tagged AHR, and HIS-tagged PML expression plasmid. Cell lysates were subjected to immunoprecipitation (IP) with anti-AHR antibodies to examine the indicated protein interaction.

(G) Schematic of the putative mechanism by which the AHR, PML, and STING1 transcriptional complexes regulate gene expression in the nucleus.

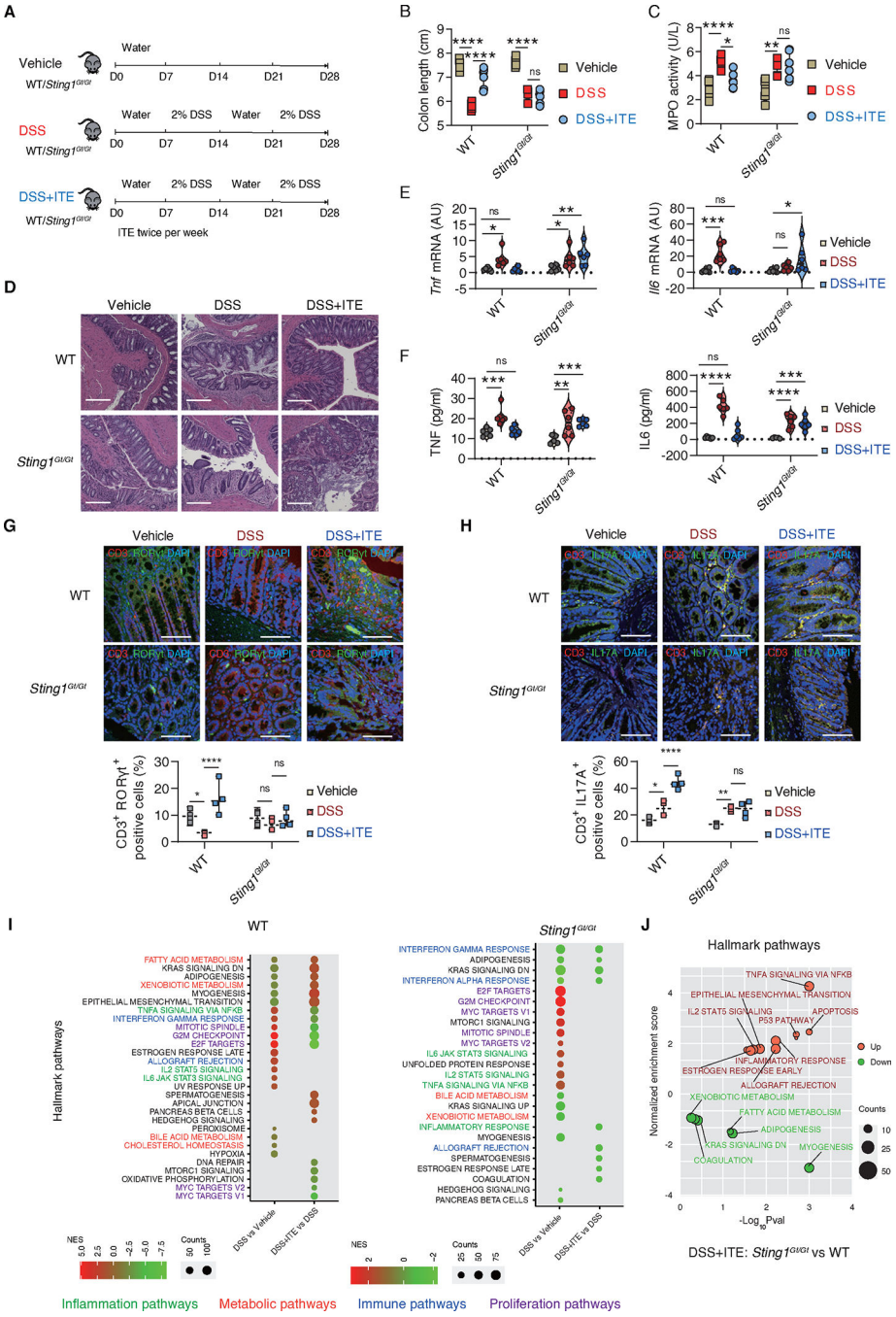

Figure 6. AHR ligands prevent DSS-induced IBD in a STING1-dependent manner, see also Figure S6.

(A) Schematic of the experimental design and drug treatments in WT and *Sting1*$^{Gt/Gt}$ mice.

(B) Analysis of colon length of WT and *Sting1*$^{Gt/Gt}$ mice (n=6 mice/group; ****P < 0.0001; two-way ANOVA with Tukey's multiple comparisons test; data are presented as mean ± SD).

(C) Analysis of MPO (myeloperoxidase) activity in colon homogenates of WT and *Sting1*$^{Gt/Gt}$ mice (n=6 mice/group; *P < 0.05, **P < 0.005, ****P < 0.0001; two-way ANOVA with Tukey's multiple comparisons test; data are presented as mean ± SD).
(D) Hematoxylin and eosin staining analysis of colon tissue of WT and *Sting1*$^{Gt/Gt}$ mice. Scale bar: 275 μm.
(E) qPCR analysis of *Tnf* and *Il6* gene expression in colon tissue from WT and *Sting1*$^{Gt/Gt}$ mice (n=6 mice/group; *P < 0.05, **P < 0.005, ***P < 0.0005; two-way ANOVA with Tukey's multiple comparisons test; data are presented as mean ± SD).
(F) ELISA analysis of TNF and IL6 in serum from WT and *Sting1*$^{Gt/Gt}$ mice (n=6 mice/group; **P < 0.005, ***P < 0.0005, ****P < 0.0001; two-way ANOVA with Tukey's multiple comparisons test; data are presented as mean ± SD).
(G) Immunofluorescence analysis of the CD3$^+$ (red) and RORγt$^+$ (green) positive cells (indicating ILC3 cells) in colon tissues from WT and *Sting1*$^{Gt/Gt}$ mice. The nuclei are stained with DAPI (blue). Scale bar: 100 μm. The semi-quantitative data are presented as the mean ± SD from 5 fields of view.
(H) Immunofluorescence analysis of the CD3$^+$ (red) and IL17A$^+$ (green) positive cells (indicating Th17 cells) in colon tissues from WT and *Sting1*$^{Gt/Gt}$ mice. The nuclei are stained with DAPI (blue). Scale bar: 100 μm. The semi-quantitative data are presented as the mean ± SD from 5 fields of view.
(I) Hallmark pathway enrichment analysis with differentially expressed genes from RNA sequencing data in the indicated WT and *Sting1*$^{Gt/Gt}$ mice. The inflammation pathways (green), metabolic pathways (red), immune pathways (blue), and proliferation pathways (purple) are highlighted (n=3 mice/group).
(J) Hallmark pathway enrichment analysis with differentially expressed genes from RNA sequencing data in WT and *Sting1*$^{Gt/Gt}$ mice treated with DSS and ITE. The upregulated and downregulated pathways are shown in red and green, respectively (n=3 mice/group).

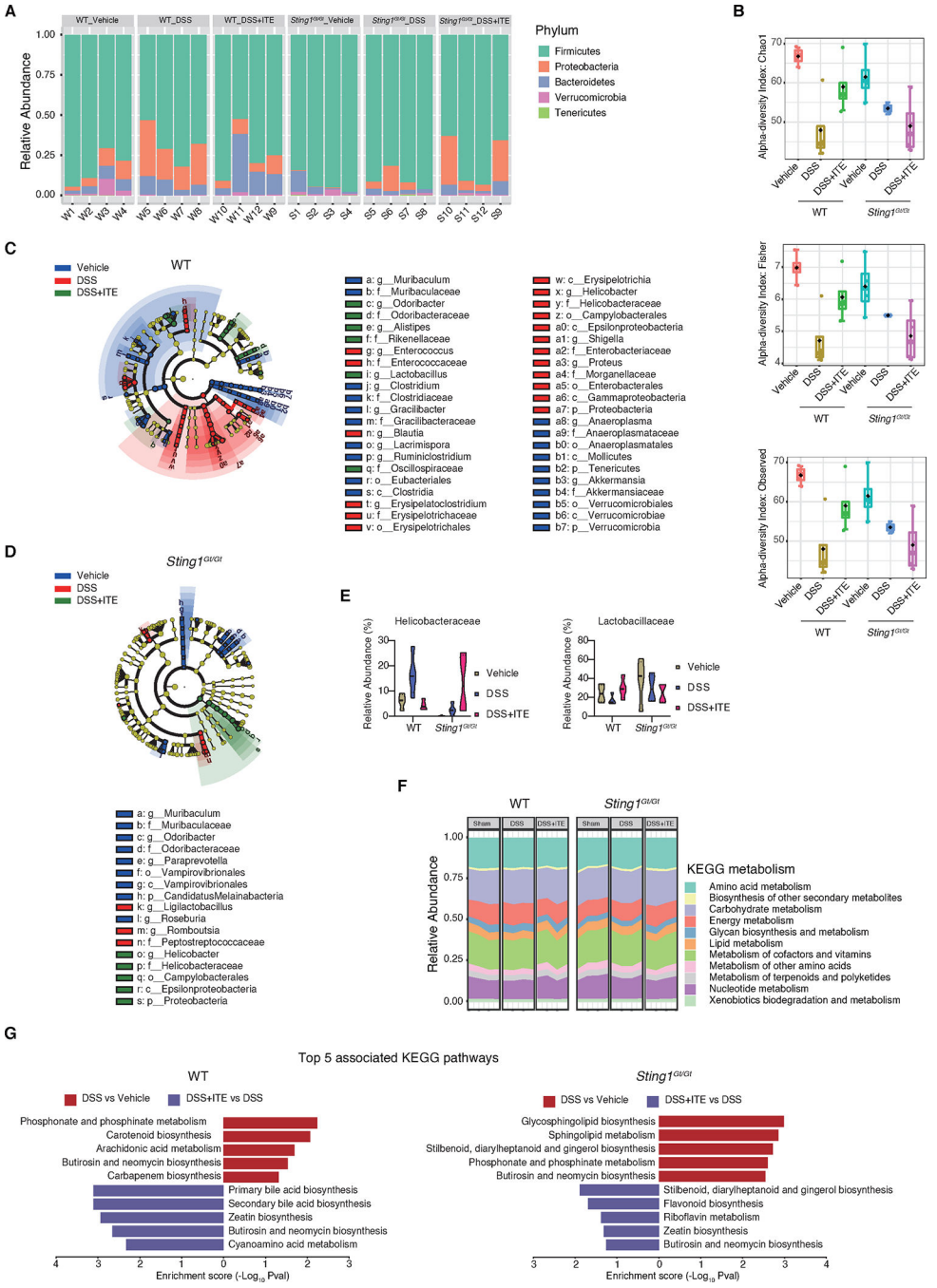

Figure 7. AHR ligands improve DSS-induced dysbiosis in a STING1-dependent manner, see also Figure S7.

(A) Fecal microbiota composition of the indicated groups in WT and *Sting1*$^{Gt/Gt}$ mice (n=4 mice/group). Relative abundance of bacteria at the phylum level.

(B) Alpha-diversity, measured by chao1, fisher, and observed species diversity index is plotted for the indicated WT and *Sting1*$^{Gt/Gt}$ mice (n=4 mice/group).

(C) Cladogram of the LEfSe analysis of the gut microbiota of the indicated groups in WT mice (n=4 mice/group). The microbial compositions were compared at different evolutionary levels.

(D) Cladogram of the LEfSe analysis of the gut microbiota of the indicated groups in *Sting1*$^{Gt/Gt}$ mice (n=4 mice/group). The microbial compositions were compared at different evolutionary levels.

(E) Relative abundance of *Helicobacteraceae* and *Lactobacillaceae* in the indicated groups in WT and *Sting1*$^{Gt/Gt}$ mice (n=4 mice/group).

(F) Comparison of KEGG metabolism pathways predicted by PICRUSt in the indicated WT and *Sting1*$^{Gt/Gt}$ mice (n=4 mice/group).

(G) The top 5 upregulated or downregulated pathways are shown in red or blue, respectively.

Key resources table

REAGENT or RESOURCE	SOURCE	IDENTIFIER
Antibodies		
Anti-STING1	Cell Signaling Technology	Cat#13647; RRID:AB_2732796
Anti-STING1	Cell Signaling Technology	Cat#50494; RRID:AB_2799375
Anti-MAP1LC3 /LC3	Cell Signaling Technology	Cat#12741; RRID:AB_2617131
Anti-ATG5	Cell Signaling Technology	Cat#12994, RRID:AB_2630393
Anti-SQSTM1/p62	Cell Signaling Technology	Cat#23214; RRID:AB_2798858
Anti-p-IRF3 (Ser386)	Cell Signaling Technology	Cat#37829; RRID:AB_2799121
Anti-p-STING1 (Ser366)	Cell Signaling Technology	Cat#19781; RRID:AB_2737062
Anti-CGAS	Cell Signaling Technology	Cat#31659; RRID:AB_2799008
Anti-IRF3	Cell Signaling Technology	Cat#4302; RRID:AB_1904036
Anti-p-TBK1 (Ser172)	Cell Signaling Technology	Cat#5483; RRID:AB_10693472
Anti-HSP90	Cell Signaling Technology	Cat#4877; RRID:AB_2233307
Anti-AHR	Santa Cruz Biotechnology	Cat#sc-133088; RRID:AB_2273721
Anti-AHR	Cell Signaling Technology	Cat#83200; RRID:AB_2800011
Anti-COX4I1/COX4	Cell Signaling Technology	Cat#4844; RRID:AB_2085427
Anti-MT-CO2/COX2	Cell Signaling Technology	Cat#4842; RRID:AB_2084968
Anti-H3C1/Histone H3	Cell Signaling Technology	Cat#9715; RRID:AB_331563
Anti-LMAN1/ERGIC53	Santa Cruz Biotechnology	Cat#sc-365158; RRID:AB_10709004
Anti-ARNT	Santa Cruz Biotechnology	Cat#sc-55526; RRID:AB_673397
Anti-DHX9	Santa Cruz Biotechnology	Cat#sc-137232; RRID:AB_2261698
Anti-XRCC6	Santa Cruz Biotechnology	Cat#sc-17789; RRID:AB_628454
Anti-RNF20	Santa Cruz Biotechnology	Cat#sc-517358
Anti-PML	Santa Cruz Biotechnology	Cat#sc-966; RRID:AB_628162
Anti-CD3	Santa Cruz Biotechnology	Cat#sc-20047; RRID:AB_627014
Anti-IL17A	Abcam	Cat#ab79056; RRID:AB_1603584
Anti-RORγt	Thermo Fisher Scientific	Cat#46–6981; RRID:AB_10717534
Anti-HA tag	Cell Signaling Technology	Cat#3724; RRID:AB_1549585
Anti-FLAG tag	Cell Signaling Technology	Cat#14793; RRID:AB_2572291
Anti-HIS tag	Cell Signaling Technology	Cat#2365; RRID:AB_2115720
Anti-GAPDH	Cell Signaling Technology	Cat#2118; RRID:AB_561053
Anti-ACTB	Cell Signaling Technology	Cat#3700; RRID:AB_2242334
Anti-IgG control	Cell Signaling Technology	Cat#5415; RRID:AB_10829607
FITC anti-mouse CD4	BioLegend	Cat#100405; RRID:AB_312691
Alexa Fluor 488 anti-mouse	Thermo Fisher Scientific	Cat#A32723; RRID:AB_2633275
Alexa Fluor 555 anti-rabbit	Thermo Fisher Scientific	Cat#A21428; RRID:AB_2535849
Alexa Fluor 488 anti-rabbit	Thermo Fisher Scientific	Cat#A11008; RRID:AB_143165
Alexa Fluor 594 anti-mouse	Thermo Fisher Scientific	Cat#A11005; RRID:AB_2534073
Anti-Mouse CD28	Invitrogen	Cat#14–0281-82

REAGENT or RESOURCE	SOURCE	IDENTIFIER
Anti-Mouse CD3ε	Invitrogen	Cat#14–0033-82
Anti-Mouse IFN-γ	R&D Systems	Cat#MAB485-SP
Anti-Mouse IL-4	R&D Systems	Cat#MAB404
Bacterial and virus strains		
Biological samples		
Chemicals, peptides, and recombinant proteins		
Mouse IL-6 protein	Miltenyi Biotec	Cat#130–094-065
Mouse IL-23 protein	Miltenyi Biotec	Cat#130–096-676
Human TGFB1 protein	Proteintech	Cat#HZ-1011
FICZ	InvivoGen	Cat#tlrl-ficz
ITE	InvivoGen	Cat#tlrl-ite
L-KYN	InvivoGen	Cat#tlrl-kyn
2’3’-cGAMP	InvivoGen	Cat#tlrl-nacga23
Dextran sulfate sodium	MP Biomedicals	Cat#02101516-CF
Lipofectamine 3000	Invitrogen	Cat#L3000–015
Puromycin	InvivoGen	Cat#ant-pr-1
SuperSignal west pico chemiluminescent substrate	Thermo Fisher Scientific	Cat#34580
SuperSignal west femto maximum sensitivity substrate	Thermo Fisher Scientific	Cat#34095
MG132	Selleck Chemicals	Cat#S2619
Cycloheximide	MedChemExpress	Cat#HY-12320
Critical commercial assays		
BCA Protein Assay Kit	Thermo Fisher Scientific	Cat#23225
Cell Counting Kit-8	Bimake	Cat#B34302
Neon Transfection System Kit	Thermo Fisher Scientific	Cat#MPK10096
Cell Fractionation Kit	Cell Signaling Technology	Cat#9038
QUANTI-Luc luciferase detection kit	InvivoGen	Cat#rep-qlcg1
NucleoBond Xtra Midi EF Kit	Macherey-Nagel	Cat#740410
E.Z.N.A. HP Total RNA Kit	Omega Bio Tek	Cat#6812–01
PrimeScript RT Reagent Kit	Takara	Cat#RR037A
SYBR Green qPCR Master Mix	Bimake	Cat#21203
Protein A magnetic beads	MilliporeSigma	Cat#LSKMAGA10
Q5® Site-Directed Mutagenesis Kit	New England Biolabs	Cat#E0554S
DNA/RNA shield	Zymo Research	Cat#R1100
Mouse Naïve CD4+ T Cell Isolation Kit	Stemcell Technologies	Cat#19765
Mouse TNF ELISA Kit	BioLegend	Cat#430907

REAGENT or RESOURCE	SOURCE	IDENTIFIER
Mouse IL6 ELISA Kit	BioLegend	Cat#4313075
Deposited data		
Raw next-generation sequencing data	This paper	NCBI SRA BioProject (accession: PRJNA902901)
Raw 16S rRNA gene sequencing data	This paper	NCBI SRA BioProject (accession: PRJNA902901)
Experimental models: Cell lines		
THP1	InvivoGen	Cat#thpd-nfis
HT29-Lucia AHR cells	InvivoGen	Cat#ht2l-ahr
IRF3$^{-/-}$ THP1 cells	InvivoGen	Cat#thpd-koirf3
CGAS$^{-/-}$ THP1 cells	InvivoGen	Cat#thpd-kocgas
STING1$^{-/-}$ THP1 cells	InvivoGen	Cat#thpd-kostg
STING1-V155M THP1 cells	InvivoGen	Cat#thpd-m155
STING1-N154S THP1 cells	InvivoGen	Cat#thpd-s154
STING1-GFP HeLa cells	This paper	N/A
HT-29 cells	ATCC	Cat#HTB-38
MEFs	ATCC	Cat#CRL-2911; RRID:CVCL_L690
Atg5$^{-/-}$ MEFs	Gonugunta et al.[64]	N/A
Sting1$^{-/-}$ MEFs	Gonugunta et al.[64]	N/A
293FT cells	Thermo Fisher Scientific	Cat#R70007
293T cells	ATCC	Cat#CRL-3216
Experimental models: Organisms/strains		
C57BL/6 WT	The Jackson Laboratory	Cat# 000664; RRID:IMSR_JAX:000664
C57BL/6J *Sting1*$^{Gt/Gt}$	The Jackson Laboratory	Cat# 017537; RRID:IMSR_JAX:017537
Oligonucleotides		
shRNAs targeting sequences, see Table S2	This paper	N/A
qPCR primers, see Table S3	This paper	N/A
Recombinant DNA		
psPAX2	Addgene	Cat#12260; RRID:Addgene_12260
pMD2.G	Addgene	Cat#12259; RRID:Addgene_12259
pCMV6-Entry-FLAG	OriGene	Cat#PS100001
pCMV6-STING1-FLAG	OriGene	Cat#RC208418
pCMV6-STING1 AA1–139-FLAG	This paper	N/A
pCMV6-STING1 AA1–180-FLAG	This paper	N/A
pCMV6-STING1 AA1–321-FLAG	This paper	N/A
pCMV6-STING1 AA1–343-FLAG	This paper	N/A
pCMV6-STING1 AA1–370-FLAG	This paper	N/A
pCMV6-STING1 AA140–379-FLAG	This paper	N/A
pCDNA3.1	Addgene	Cat#128023, RRID:Addgene_128023
pCDNA3.1-AHR-HA	This paper	N/A
pCDNA3.1-AHR AA1–400-HA	This paper	N/A

REAGENT or RESOURCE	SOURCE	IDENTIFIER
pCDNA3.1-AHR AA401–848-HA	This paper	N/A
pPM-PML-HIS	Applied Biological Materials	Cat#370640210600
Software and algorithms		
Image Lab software	Bio-Rad	http://www.bio-rad.com/en-us/sku/1709690-image-lab-software; RRID:SCR_014210
GraphPad Prism 9.0	GraphPad Software	http://www.graphpad.com/; RRID:SCR_002798
FlowJo software 9.0	BD Biosciences	https://www.flowjo.com/solutions/flowjo; RRID:SCR_008520
CB-Dock2	Liu et al.[97]	https://cadd.labshare.cn/cb-dock2/php/index.php
PISA interface server	PISA interface server Software	https://www.ebi.ac.uk/pdbe/pisa/; RRID:SCR_015749
GSEA	GSEA Software	http://www.broadinstitute.org/gsea/; RRID:SCR_003199
g:Profiler	ELIXIR infrastructure	http://biit.cs.ut.ee/gprofiler/; RRID:SCR_006809
iDEP	Ge et al.[102]	http://bioinformatics.sdstate.edu/idep/
MicrobiomeAnalyst	MicrobiomeAnalyst software	https://www.microbiomeanalyst.ca/; RRID:SCR_015022
ImageGP	Chen et al.[106]	http://www.ehbio.com/
Other		